



HAL
open science

Temporal variations in porewater fluxes to a coastal lagoon driven by wind waves and changes in lagoon water depths

Valenti Rodellas, Peter Cook, James Mccallum, Aladin Andrisoa, Samuel Meulé, Thomas Stieglitz

► To cite this version:

Valenti Rodellas, Peter Cook, James Mccallum, Aladin Andrisoa, Samuel Meulé, et al.. Temporal variations in porewater fluxes to a coastal lagoon driven by wind waves and changes in lagoon water depths. *Journal of Hydrology*, 2020, 581, 10.1016/j.jhydrol.2019.124363 . hal-02392263

HAL Id: hal-02392263

<https://amu.hal.science/hal-02392263>

Submitted on 3 Dec 2019

HAL is a multi-disciplinary open access archive for the deposit and dissemination of scientific research documents, whether they are published or not. The documents may come from teaching and research institutions in France or abroad, or from public or private research centers.

L'archive ouverte pluridisciplinaire **HAL**, est destinée au dépôt et à la diffusion de documents scientifiques de niveau recherche, publiés ou non, émanant des établissements d'enseignement et de recherche français ou étrangers, des laboratoires publics ou privés.

1 **Temporal variations in porewater fluxes to a coastal lagoon driven by wind waves**
2 **and changes in lagoon water depths**

3

4 Valentí Rodellas^{1,2*}, Peter G. Cook^{3,4}, James McCallum⁵, Aladin Andrisoa¹, Samuel Meulé¹,
5 Thomas C. Stieglitz^{1,6}

6

7 ¹Aix-Marseille Univ, CNRS, IRD, INRA, Coll France, CEREGE, 13545 Aix-en-Provence, France

8 ²Institut de Ciència i Tecnologia Ambientals (ICTA), Universitat Autònoma de Barcelona, E-08193
9 Bellaterra, Catalonia, Spain

10 ³National Centre for Groundwater Research and Training (NCGRT), School of the Environment,
11 Flinders University, Adelaide SA 5001, Australia

12 ⁴Aix-Marseille Université, IMÉRA, 13000 Marseille, France

13 ⁵School of Earth Sciences, The University of Western Australia, Perth WA 6009, Australia

14 ⁶Centre for Tropical Water and Aquatic Ecosystem Research, James Cook University, Townsville,
15 Queensland 4811, Australia

16

17 *Corresponding Author: Valentí Rodellas (valenti.rodellas@uab.cat)

18 **ABSTRACT**

19 Porewater fluxes, including fresh groundwater discharge and circulation of surface
20 waters through sediments, are increasingly documented to play an important role in
21 hydrological and biogeochemical cycles of coastal water bodies. In most studies, the
22 magnitude of porewater fluxes is inferred from geochemical tracers, but a detailed
23 understanding of the underlying physical forces driving these fluxes remains limited. In
24 this study, we evaluate the mechanisms driving porewater fluxes in the shallow coastal
25 La Palme lagoon (France). We combined measurements of variations of salinity and
26 temperature in the subsurface with 1-dimensional fluid, salt and heat transport models to
27 evaluate the dynamics of porewater fluxes across the sediment-water interface in
28 response to temporally variable forcings. Two main processes were identified as major
29 drivers of porewater fluxes: i) temporal variations of lagoon water depths (forcing
30 porewater fluxes up to 25 cm d⁻¹) and ii) locally-generated wind waves (porewater fluxes
31 of ~50 cm d⁻¹). These processes operate over different spatial and temporal scales; Wind-
32 driven waves force the shallow circulation of surface lagoon waters through sediments
33 (mostly < 0.2 m), but are restricted to strong wind events (typically lasting for 1-3 days).
34 In contrast, porewater fluxes driven by variations of lagoon water depths flush a much
35 greater depth of sediment (>1 m). The spatial and temporal scales of driving forces will
36 largely determine the significance of porewater fluxes, as well as their chemical
37 composition. Thus, an appropriate evaluation of the magnitude of porewater-driven
38 solute fluxes and their consequences for coastal ecosystems requires a solid and site-
39 specific understanding of the underlying physical forces.

40

41 **Keywords:** porewater exchange, submarine groundwater discharge, coastal lagoon,
42 driving forces, waves, salinity, temperature

43 **1. INTRODUCTION**

44 Water fluxes circulating through permeable sediments are increasingly being recognized
45 as an important source of dissolved solutes (e.g. nutrients, metals, pollutants) to surface
46 water bodies (Anschutz et al., 2009; Liefer et al., 2013; Rodellas et al., 2015). In coastal
47 settings, these fluxes across the sediment-water interface are commonly referred to as
48 Submarine Groundwater Discharge (SGD) or porewater exchange (PEX), depending on
49 the scale of the circulation process (Moore, 2010; Santos et al., 2012). In this study, we
50 use the term porewater fluxes to refer to the total efflux of water and solutes across the
51 permeable sediments to surface waters, thus including both SGD and PEX. Porewater-
52 driven fluxes of solutes may exert a major control on the biogeochemistry, water quality
53 and ecological functioning of receiving water bodies, e.g. contributing to sustaining the
54 primary production and community composition of phytoplankton in coastal areas
55 (Andrisoa et al., 2019; Garcés et al., 2011; Valiela et al., 1990), promoting eutrophication
56 of surface waters (Hwang et al., 2005; Paerl, 1997), and leading to recurrent harmful algal
57 blooms (Gobler and Sañudo-Wilhelmy, 2001; Lee et al., 2010).

58
59 The physical mechanisms driving porewater fluxes strongly affect the residence time of
60 waters within sediments or the coastal aquifer, determining the extent and rates of
61 biogeochemical reactions and therefore the composition of discharging fluids (Santos et
62 al., 2012; Weinstein et al., 2011). An appropriate understanding of the magnitude of
63 solute fluxes driven by groundwater and porewater discharge requires thus identifying
64 the mechanism forcing these inputs. Many physical processes produce pressure gradients
65 at the sediment-water interface that can force advective porewater fluxes. The main
66 driving forces include the terrestrial hydraulic gradient and its seasonal oscillations,
67 wave and tidal pumping, the interaction of currents and seafloor topography, convection

68 driven by density inversions or pumping activities of benthic fauna (Huettel et al., 2014;
69 Santos et al., 2012). These different forcing mechanisms, which are of both marine (e.g.
70 wave and tidal setup) and terrestrial (e.g. hydraulic gradient) origin, are highly dynamic
71 and irregular, span a wide range of exchange lengths and timescales and are frequently
72 superimposed (Robinson et al., 2017; Santos et al., 2012, 2009).

73
74 A large number of studies highlight the overall magnitude and the significance of
75 porewater fluxes (e.g. (Cho et al., 2018; Kwon et al., 2014; Moore et al., 2008; Rodellas et
76 al., 2015)), but there is still little information about their driving forces (Robinson et al.,
77 2017). Studies conducted to date have evaluated the effect of individual driving forces in
78 isolation and have been mainly focused on regular and short-term forces (e.g. semi-
79 diurnal/diurnal tides, density-driven flows), mainly as a consequence of the difficulties
80 inherent in investigating irregular and longer period forcing via field experiments and in
81 unraveling the various forcing effects (Robinson et al., 2017). Irregular forcings, such as
82 episodic, high intensity events, may have a great impact on fluxes of water and solutes
83 driven by porewater fluxes (Sawyer et al., 2013; Smith et al., 2008). The understanding of
84 these forcing is thus required to better predict the effects of increasing stressors in the
85 system (e.g. climate change, anthropogenic pressure) and to better identify settings
86 where specific forcings may dominate over the others.

87
88 This study is aimed at characterizing porewater fluxes in a shallow coastal lagoon (La
89 Palme Lagoon, France), where the circulation of significant volumes of surface water
90 through sediments have been previously documented (Cook et al., 2018a; Rodellas et al.,
91 2018; Stieglitz et al., 2013; Tamborski et al., 2018). These previous studies have
92 estimated the average magnitude of porewater fluxes to the lagoon, but they provided

93 little insight into their temporal variations and the mechanisms driving these fluxes. The
94 current paper examines variations of subsurface temperature and porewater salinity in
95 La Palme lagoon to evaluate the dynamics of porewater fluxes and to provide some
96 insight into controlling forcings. In this study, we focus on two mechanisms that can
97 control porewater fluxes in the lagoon and that operate over different temporal and
98 spatial scales: i) the variations of lagoon water depths, which can influence the terrestrial
99 hydraulic gradient and drive long-scale (>1 m) porewater fluxes, and ii) wave pumping
100 produced by the strong winds of the region, which forces the flushing of shallow
101 sediments (short-scale porewater fluxes). Other active mechanisms are likely
102 significantly contributing to total porewater fluxes (e.g. bioirrigation or current-
103 topography interactions), but they are not specifically evaluated in this study.
104

105 2. METHODS

106 2.1. Study site: La Palme lagoon, France

107 La Palme is a small (500 ha surface area), shallow coastal lagoon, with mean and
108 maximum water depths of ~ 0.7 and ~ 2 m, respectively (Fig. 1). It is connected with the
109 Mediterranean Sea through a small opening in the coastal sand spit, which may be
110 seasonally closed, and it receives continuous fresh groundwater inputs ($0.01 - 0.04 \text{ m}^3 \text{ s}^{-1}$)
111 ¹⁾ mainly from a regional karst aquifer, constituted by karstified Jurassic and Lower
112 Cretaceous limestones (Stieglitz et al., 2013; Wilke and Boutière, 2000). The lagoon is also
113 connected with a shallow alluvial aquifer (Alluvial aquifer of Aude and Berre rivers), but
114 little information is available on the aquifer-lagoon interaction. The internal mixing of the
115 lagoon and its exchange with coastal waters is driven primarily by the strong north-
116 westerly winds characteristic of the region (regularly exceeding 10 m s^{-1}). Given that tidal
117 variations in the Mediterranean Sea are usually small and the exchange between La
118 Palme lagoon and the sea is highly restricted by three physical barriers (railway dike,
119 road dike and sandy barrier; Fig. 1), tidal forcing plays a minor role on the hydrodynamic
120 functioning of this lagoon (tidal range in the lagoon $< 1 \text{ cm}$; (Fiandrino et al., 2012)). Most
121 of the lagoon is covered by fine-to-coarse grained sands ($100\text{-}500 \mu\text{m}$) and only the
122 northern part of the lagoon is dominated by fine-grained sediments ($\sim 50 \mu\text{m}$). The
123 eastern part of the lagoon is surrounded by evaporation ponds, but there is no visual or
124 chemical evidence of a connection between the lagoon and the salt pond (Rodellas et al.,
125 2018; Tamborski et al., 2018).

126
127 A study conducted by Stieglitz et al. (2013) hypothesized that strong winds produced
128 circulation of large amounts of lagoon water through surface sediments. Different studies
129 have estimated porewater inputs to the entire lagoon at $0.4 - 2.1 \text{ m}^3 \text{ s}^{-1}$ ($0.8 - 4.1 \text{ cm d}^{-1}$),

130 which is the equivalent of the volume of the entire lagoon circulating through the
131 sediments every 20 - 90 days (Rodellas et al., 2018; Stieglitz et al., 2013; Tamborski et al.,
132 2018). However, to date, the forces driving these fluxes have not been evaluated in detail.

133

134 **2.2. Sampling and analysis**

135 Four different stations (Pz1, Pz2, Pz3, Pz4) were established in areas considered
136 representative of the different sediment types of the lagoon (Fig 1). In May 2017, a
137 sediment core (up to 50 cm depth) was collected at each one of these locations and sliced
138 every 5 cm. The grain size distribution of each sediment sample was determined through
139 a Coulter LS230 laser diffraction particle size analyzer. Average sediment porosities for
140 each location were obtained from Tamborski et al. (2018), who collected sediment cores
141 at the same locations. Sensors for measuring temperature, salinity, lagoon water depths
142 and wave parameters were also installed at these sites and porewater samples were
143 collected, as discussed in the following sections.

144

145 Hourly rainfall, temperature, wind (speed and direction) and atmospheric pressure data
146 at the nearby meteorological station “Leucate” was extracted from the database of the
147 French meteorological service (Météo France). Additional monthly data on lagoon water
148 depths and salinity at three sites in the northern lagoon (PN stations in Fig. 1) was
149 obtained from the database of “Parc Naturel Régional de la Narbonnaise en
150 Méditerranée” (PNRNM). Data on daily piezometric levels of the alluvial aquifer
151 connected to the lagoon (Alluvial aquifer of Aude and Berre rivers) was obtained from the
152 French Groundwater National Portal (piezometer code BSS002LRH; ades.eaufrance.fr).

153

154 **2.2.1. Subsurface salinity time series**

155 Porewater samples for salinity analysis were collected during 7 different sampling
156 campaigns between March 2016 and June 2017 (March, April, June, October and
157 November 2016; April and June 2017). During each campaign, porewater samples were
158 collected from 3 different locations (Pz1, Pz2 and Pz3) using a direct-push, shielded-
159 screen well-point piezometer (Charette and Allen, 2006). Porewater samples for salinity
160 analysis (10 mL) were collected at depths ranging from 5 to 140 cm below the sediment-
161 water interface (including surface water) and measured using a pre-calibrated WTW
162 multiparameter sonde (WTW Multi 3430 meter with TetraCon® 925 probe).

163
164 A CTD logger (LTC Levellogger® from Solinst®) was installed at Pz1 from 1st April 2017
165 to 31st December 2017 at 10 cm above the sediment-water interface to monitor water
166 level (measurements were corrected for atmospheric pressure) and salinity variations in
167 surface waters. Additionally, a CTD logger (LTC Levellogger® from Solinst®) was placed
168 at 30 cm below the sediment-water interface to record changes in porewater salinities at
169 this depth for the same period. This logger was driven into sediments by using a plastic
170 rod with a shielded protection to avoid clogging of the conductivity cell (which was also
171 protected with a membrane) during installation and to minimize the disturbance of
172 sediments. Changes in pressure were also recorded at 30 cm below the sediment-water
173 interface, but water level gradients between this depth and surface water were too small
174 to be measured.

175

176 **2.2.2. Subsurface temperature time series**

177 In situ temperature data was acquired by a string of Thermochron iButton© thermistors
178 (Measuring Systems Ltd), which are small-size, stand-alone and inexpensive temperature
179 loggers with a reported accuracy of $\pm 0.2^{\circ}\text{C}$ and a resolution of 0.06°C (Johnson et al.,

180 2005). The sensors were placed at depths of 5, 10, 15, 25 and 40 cm below the sediment-
181 water interface and at 10 cm above the seafloor by vertically driving a 2 cm diameter
182 wooden rod (with the thermistors inserted) into the sediments. These strings of
183 thermistors were installed simultaneously at each of the above 4 locations in La Palme
184 lagoon (Pz1, Pz2, Pz3, Pz4) during 2 periods of ~1 month (between May 9 and May 30,
185 and between June 9 and July 5). The strings of thermistors were also installed between
186 November and December 2017, but the data obtained from this deployment is not
187 included in this manuscript because it was a period of abrupt changes in lagoon water
188 depths which makes interpretation of the data difficult. Once recovered, the thermistors
189 were intercalibrated in a calibration bath. During the deployment periods, pressure
190 sensors (NKE, SP2T10) were installed at stations Pz1, Pz2 and Pz3 measuring water
191 depths for 5 minutes per hour at a frequency of 4Hz to monitor the variability of wave
192 parameters (significant wave height and period) and water depths. A barometer
193 (Barologger Edge from Solinst®) was also installed in La Palme lagoon to correct water
194 pressures for changes in atmospheric pressure.

195

196 **2.3. Numerical modeling**

197 **2.3.1. Numerical modeling of subsurface salinities to estimate deep porewater**

198 **fluxes**

199 Models of salt transport have been used to estimate the exchange of water and solutes
200 across the sediment-water interface, where surface and porewaters have distinctive salt
201 concentrations (Martin et al., 2007, 2004; Morris, 1995; Rapaglia and Bokuniewicz,
202 2009). A vertical one-dimensional finite element model was developed to investigate
203 porewater fluxes from the subsurface to the lagoon, based on the equations of (Simmons
204 et al., 2001; Voss and Souza, 1987). The fluid mass balance equation is:

205
$$\rho S_{op} \frac{\partial p}{\partial t} + \theta \frac{\partial \rho}{\partial C} \frac{\partial C}{\partial t} + \frac{\partial}{\partial z} (\theta \rho v) = Q_p \quad (1)$$

206 where ρ is the fluid density [kg m^3], S_{op} is the compressibility of the saturated sediment
 207 [Pa^{-1}], p is pressure [Pa], θ is the porosity [dimensionless], C is the concentration of the
 208 chemical species (salt) [kg m^{-3}], Q_p is the water source or sink [$\text{kg m}^{-3} \text{ s}^{-1}$] and v is the fluid
 209 velocity [m s^{-1}] defined as:

210
$$v = - \left(\frac{k}{\mu \theta} \left[\frac{\partial p}{\partial z} - \rho g \right] \right) \quad (2)$$

211 where k is the permeability of the sediment [m^2], μ is the viscosity of the fluid [Pa s] and g
 212 is the gravitational constant [9.8 m s^{-2}],

213

214 To simulate the movement of the solute species (salt, in this case), Equation 1 is coupled
 215 to the transport equation (Simmons et al., 2001; Voss and Souza, 1987):

216
$$\theta \rho \frac{\partial C}{\partial t} + \frac{\partial}{\partial z} \theta \rho v C - \frac{\partial}{\partial z} \left(\theta \rho D \frac{\partial C}{\partial z} \right) = Q_p (C_p - C) \quad (3)$$

217 where D is the dispersion coefficient [$\text{m}^2 \text{ s}^{-1}$] and C_p is the concentration of solute species
 218 (salt) in the fluid source [kg m^{-3}].

219

220 The equations were solved with a Galerkin finite element numerical technique using one-
 221 dimensional linear element, which was implemented in Python using the NumPy and
 222 SciPy libraries (Oliphant, 2007; van der Walt et al., 2011). The fluid (Eq. 1) and solute (Eq.
 223 3) transport equations were solved iteratively until the residuals for both pressure and
 224 concentration were $<10^{-9}$. The term $\partial \rho / \partial C$ was assumed to be a constant value.

225

226 Parameter values used in the one-dimensional model are shown in Table 1. The model
 227 was assumed to be homogeneous, with uniform properties for permeability, viscosity,
 228 porosity and dispersity. The model implemented boundary conditions of pressure and

229 concentration at both the top and bottom node of the model, with pressure approximated
230 as $p \approx \rho gh$. The water flux exchanged across the sediment-water interface (cm d^{-1} or cm^3
231 $\text{cm}^{-2} \text{d}^{-1}$) was assessed by determining the Darcy flux ($v \theta$) in the uppermost element. The
232 model was set with element length of 0.05 m between the lagoon bed and 1 m depth, 0.1
233 m between 1 and 2 m, and 0.2 m between 2 and 4 m depth. These depths were chosen so
234 that nodes were coincident with the location of porewater observations. The upper
235 pressure and salinity boundary conditions were taken from measured values in the
236 lagoon (see 2.2.1); Between 21st January 2016 and 29th June 2017, boundary conditions
237 were obtained by linearly interpolating between monthly measurements in station PN1.
238 Between 29th June 2017 and 31st December 2017, the salinity and pressure values were
239 obtained from the CTD logger installed in the surface water at station Pz1 (see 2.2.1). The
240 lower boundary condition was fixed at a constant salinity for the duration of the
241 simulation; however, the lower pressure boundary was linearly varied over 6-month
242 periods as part of model calibration. Notice that the variations in lower pressure
243 boundary essentially represent variations in the inland groundwater head that are
244 transmitted to lagoon sediments. The model was implemented with a 4-hours time step
245 with a total simulation period of two years.

246
247 Calibration was undertaken by fitting the model results to the porewater depth profiles
248 and the CTD logger data at 0.3 m depth. All of the parameters were fixed for the
249 calibration, with the exception of h_{bot} , C_{bot} , k , θ and α . Calibration was undertaken using
250 the truncated Newton method (Nash, 1984), implemented in SciPy (Oliphant, 2007). The
251 adjustable parameters (h_{bot} , C_{bot} , k , θ and α) were modified to reduce the misfit between
252 the modeled and observed values of salinity at depth. This model was only implemented
253 at station Pz1 because it was the only station where all the input data needed for the

254 model was collected (e.g. porewater depth profiles, surface salinities and water depths,
255 continuous data at 0.3 m). The initial concentration profile was determined by linearly
256 interpolating between the measured concentrations and the lower boundary conditions
257 to produce a continuous concentration profile. This initial concentration profile was used
258 to generate a steady state pressure distribution in the profile to use as the starting
259 conditions for the transient model simulation. This was achieved by solving Eq. 1 where
260 the variation of concentration and pressure with time were set to zero.

261

262 **2.3.2. Numerical modeling of subsurface temperatures to estimate shallow** 263 **porewater fluxes**

264 Heat has been used as an environmental tracer for investigating groundwater, porewater
265 and surface water interactions in a range of hydrogeologic settings (Boano et al., 2014;
266 Cranswick et al., 2014; Martin et al., 2006; Savidge et al., 2016). Its application is based on
267 temperature differences between surface water bodies, which are subject to diel or
268 seasonal temperature variations, and porewater or groundwaters, which typically display
269 reduced temperature variation (Cranswick et al., 2014). Most of the studies have applied
270 the heat transport equation in thermal porewater records to estimate groundwater
271 advection. However, it can also be applied to estimate shallow rapid porewater exchange
272 by using a 1-D enhanced dispersion term that includes (aside from thermal conductivity)
273 an effective dispersion term accounting for the increase of heat transport driven by
274 porewater exchange (Bhaskar et al., 2012; Wilson et al., 2016). In a system without net
275 groundwater advection, the enhanced dispersion coefficient can be obtained using:

$$276 \quad \frac{\partial T}{\partial t} = D_e \frac{\partial^2 T}{\partial z^2} \quad (4)$$

277 where T is temperature, t is time, z is depth and D_e is the enhanced dispersion coefficient.

278

279 A finite difference model was written in Fortran 95 to solve Eq. 4. Rather than calibrating
280 the model to observed temperatures at all depths simultaneously, we chose to calibrate
281 temperature at each depth separately for discrete 48-hour periods with relatively
282 constant wave conditions. A period of 48 hours was chosen because periods of high wind
283 of much longer duration did not occur during our periods of measurement and shorter
284 periods are less likely to induce significant temperature changes in the subsurface. To
285 evaluate the relevance of wave pumping as a driver of porewater fluxes, several 48-hour
286 periods during the different monitoring periods were selected to represent both high and
287 low wind (wave) conditions.

288
289 Although shallow porewater fluxes are likely to produce an effective dispersion
290 coefficient that decreases with depth (Qian et al., 2009; Wilson et al., 2016), we model the
291 data using a constant dispersion coefficient, but model the temperature at each depth
292 separately. The best-fit dispersion coefficient (D_e) therefore represents a combination of
293 conduction and the apparent dispersion coefficient due to porewater exchange fluxes, to
294 the relevant depth. The model was run for each of the selected 48-hour periods, and each
295 piezometer and depth using different values of D_e (in increments of $3.5 \cdot 10^{-4} \text{ m}^2 \text{ d}^{-1}$). The
296 lowest RMSE (Root Mean Square Error) value in each case identified the best-fit value of
297 D_e . Uncertainties associated with dispersion coefficients were estimated based on the
298 shape of the RMSE versus D_e plot for each piezometer and each 48-hour period.

299 Considering the accuracy of the temperature sensors ($0.2 \text{ }^\circ\text{C}$), upper and lower bounds
300 were defined by RMSE values $0.1 \text{ }^\circ\text{C}$ greater than the minimum RMSE in each case.

301 Considering the little dependence of thermal conductivity on salinity (Caldwell, 1974), we
302 assume that variations of porewater salinities have a negligible influence on the
303 computations.

304

305 The time for temperature changes in surface water to propagate into the subsurface can
306 be expressed as:

307
$$t = \frac{z^2}{4D_e} \quad (5)$$

308 Thus, for $D_e = 4 \cdot 10^{-2} \text{ m}^2 \text{ d}^{-1}$ (a typical value for enhanced dispersion coefficient due to
309 wind and wave action; see below), the time for surface water temperature changes to
310 propagate to depths (z) of 5, 10, 15, 25 and 40 cm (depths at which sensors were
311 installed) is 0.4, 1.5, 3.3, 9.3 and 24 hours, respectively. We thus chose to focus on depths
312 of 10 and 15 cm, as temperatures at greater depths do not respond sufficiently to wave
313 conditions within the 48-hour period. We also discarded the sensors at 5 cm because of
314 uncertainties in the depth of installation and the potential effects of artifacts associated
315 with the installation of the wooden rod (e.g. alteration of sediment-water interface).

316

317 To calibrate the model, the upper boundary condition was specified as the measured
318 surface water temperature (sensor at 10 cm above the sediment-water interface), and a
319 constant temperature (20 °C) was specified at a depth of 20 m. The initial condition was
320 specified to be the measured temperatures at the start of each period, with linear
321 interpolation between observation depths. Initial temperatures between the deepest
322 sensor and the model lower boundary at 20 m were also determined by linear
323 interpolation between the deepest measurement and the specified lower boundary
324 temperature. Varying the temperature value of the lower boundary confirmed that this
325 did not affect simulated temperatures at the observation depths. Depth discretisation was
326 0.005 m, and temporal discretisation was $3.5 \cdot 10^{-5} \text{ d}$ (0.05 min).

327

328 Fig. 2 shows how different values of D_e affect time series of temperature at 15 cm depth.
329 Lower D_e values result in reduced diurnal variations and increased lag between
330 temperature minimum and maximum values in the surface water and in the subsurface.
331 Simulation of subsurface temperature and comparison with measured values hence
332 allows D_e to be estimated.

333
334 Enhanced dispersion coefficient (D_e) estimated following this approach include both
335 thermal conductivity ($D_{e(cond)}$) and dispersion due to advective porewater exchange
336 ($D_{e(adv)}$). $D_{e(cond)}$ at each station can be derived from the following equation (Irvine et al.,
337 2015; Wilson et al., 2016):

338

$$339 \quad D_{e(cond)} = \frac{K_b}{(1-\theta)\rho_s c_s + \theta\rho_w c_w} = \frac{K_s^{(1-\theta)} \cdot K_w^\theta}{(1-\theta)\rho_s c_s + \theta\rho_w c_w} \quad (6)$$

340

341 where K_b is the bulk thermal conductivity of sediments, K_s , c_s and ρ_s are the thermal
342 conductivity, specific heat capacity and density of the solid phase, respectively, K_w , c_w and
343 ρ_w are the corresponding terms for the water phase and θ is the sediment porosity.

344

345 **3. RESULTS**

346 **3.1. Sediment analysis**

347 The grain size distributions of the 4 sediment cores collected in La Palme lagoon are
348 shown in Supplementary Information (Table S1). The contents of silt and clay in
349 sediments from Pz1, Pz2 and Pz3 were low, generally below 10-15 %. Sediments from
350 these three sites were mainly composed of fine and medium-size sands. In contrast,
351 sediments from Pz4 mainly comprised silt (>40 %) and had a significant clay content (>
352 15 %). The grain size was relatively constant with depth, with the only exception being
353 Pz3, which included a layer (from ~30 to ~40 cm) with a higher content of silts and clays
354 (> 20 %). Estimated sediment permeabilities from the grain size distribution and sorting
355 following (Berg, 1970) were on the order of 10^{-10} - 10^{-11} m² for Pz1, Pz2 and Pz3 and 10^{-15}
356 m² for Pz4. Sediments from Pz1, Pz2 and Pz3 are thus characterized by a relatively high
357 permeability (Huettel et al., 2014), whereas Pz4 were lower permeability sediments.
358 Average porosities (θ) were 0.47, 0.43, 0.39 and 0.70 for Pz1, Pz2, Pz3 and Pz4,
359 respectively (Tamborski et al., 2018).

360

361 **3.2. Wind, wave and lagoon water depth dynamics**

362 The region is characterized by frequent strong winds (>10 m s⁻¹) generally blowing from
363 the N-W (locally called “Tramontane”) and sporadic winds from the sea (S-E) that can
364 also reach high speeds and that are usually linked to storms. Indeed, in 2017, most events
365 where wind speed exceeded 10 m s⁻¹ were blowing either from the NW (59%) or the SE
366 (37%). The time series of wind speeds during the main period of samplings (April 2017 –
367 December 2017) is shown in Fig 3.a.

368

369 Water depths in the lagoon decreased progressively from April to September 2017 (from
370 ~0.9 to ~0.4 m in Pz1; Fig 3.b.), mainly as a consequence of an increase in temperatures
371 and a reduction of precipitation and groundwater inputs that resulted in evaporative
372 losses exceeding water inputs (Rodellas et al., 2018). During this period, wind dynamics
373 exerted a minor control on the water depths of the lagoon and were only responsible for
374 water depth oscillations (< 0.5 m) that lasted for less than 24 hours. Significant changes
375 in lagoon water depths were measured between 15th-20th October (predominantly SE
376 winds) and 6th-15th November (NW winds), as a consequence of strong wind events that
377 opened the sandy barrier that separates the lagoon from the sea (which remained open
378 for a few days after the wind event): lagoon water in the northern basin increased by
379 ~0.2 m in October as a consequence of the SE wind event, which brought water from the
380 central and southern basins (and the Mediterranean Sea), and it decreased by ~0.15 m in
381 November due to NW winds. After these events the sandy barrier became less
382 consolidated and thus more permeable to water exchange and most of the subsequent
383 wind events produced significant changes in lagoon water depths.

384
385 The generation of waves in the lagoon is highly controlled by the wind regime (direction,
386 speed and duration), as evidenced by the similar wind and wave patterns (Fig. 4). During
387 calm periods, wave height remained below 0.02 m. Strong wind events produced rapid
388 increases of wave heights (wave height up to 0.10 m; wave period of 1-2 s), which
389 remained elevated for the duration of the event. No major differences in wave height and
390 period were observed between the different sampling stations (Pz1, Pz2 and Pz3), which
391 were located in different areas of the lagoon. The spectral analysis of lagoon water depths
392 revealed that the influence of seiches and tides was negligible at La Palme lagoon for the

393 studied periods. We thus exclude them as drivers of porewater fluxes for La Palme
394 lagoon.

395

396 **3.3. Porewater salinities**

397 Porewater could be easily sampled with a push-point piezometer from most of the depths
398 at the locations Pz1, Pz2 and Pz3, indicating a relatively high hydraulic permeability for
399 the sandy sediments at these locations. The only exception was a low permeability layer
400 found at Pz3, extending from ~30 to ~40 cm below the sediment-water interface (see
401 section 3.1.). Porewater samples could not be collected at Pz4 due to the low hydraulic
402 conductivities, which is consistent with the low permeabilities derived from sediment
403 core particle size analysis (see section 3.1.). Salinities in porewater mainly reflect a
404 mixing between two endmembers (Fig. 5): i) lagoon waters with varying salinities
405 depending on the season and the location (salinities usually between 20 and 40) and ii)
406 deep hypersaline porewaters, with salinities above 80, most likely from an evaporative
407 origin (Fig. 5). As a consequence, porewater salinities generally increased downwards,
408 although these trends depend on the dynamics of this 2-endmember mixing, which varies
409 significantly depending on the sampling time and location.

410

411 **3.3.1. Estimation of advective vertical velocities from subsurface salinities**

412 The significantly greater salinities measured in deep porewater than in shallow
413 porewaters produce deep porewaters being significantly denser than overlying fluids
414 (notice that temperature differences between surface and deep waters (differences < 10
415 °C) have a minor influence on fluid density differences in comparison to the controls
416 played by salinity differences). These conditions produce stable density profiles that
417 prevent gravitational convection or salt fingering (Bokuniewicz et al., 2004; Simmons et

418 al., 2001). However, the variability of salinity in porewaters observed at each site during
419 the different sampling periods (Fig. 5) suggests that porewater advection (driven by
420 hydraulic head gradients) exerts a major control on the vertical profiles. Subsurface
421 salinity variations can be used to assess the magnitude of porewater advection (i.e. deep
422 porewater fluxes) and their temporal variability by applying the fluid and salt transport
423 one-dimensional model described in section 3.2.1, which accounts for both density and
424 hydraulic gradient differences.

425
426 The results of the observed and modeled subsurface salinities for station Pz1 are shown
427 in Figures 6 and 7, and include both the porewater profiles collected at different periods
428 (Fig. 6) and the continuous measurements at 30 cm below the sediment-water interface
429 (Fig. 7). The model reproduces the observed subsurface salinities remarkably well,
430 particularly for the observations at 30 cm below the sediment-water interface. Some
431 differences between observed and model salinities at the shallow area of the porewater
432 profiles might be related to mechanisms driving shallow and rapid lagoon water-
433 porewater exchange (e.g. increase porewater fluxes driven by wave pumping or
434 bioirrigation) that are not accounted for in the advection-dispersion model. It should also
435 be noted that these results are also limited by the boundary conditions, which were
436 assumed i) to vary linearly between monthly measurements at the top (continuously
437 measured for the last ~6 months), and ii) to be constant for salinity and vary linearly over
438 6-months periods for pressure at the lower boundary.

439
440 The modeled vertical porewater fluxes needed to reproduce the observed subsurface
441 salinities using the lagoon water depths and salinities measured in surface water are
442 shown in Figure 8. Estimated porewater advection (darcy) fluxes range from -11 to 25 cm

443 d^{-1} , with positive fluxes representing porewater fluxes to the lagoon and negatives values
444 the infiltration of lagoon water to the sediments. These modeled porewater advection
445 rates for station Pz1 show a correspondence with lagoon water depths (Fig. 8): negligible
446 or negative porewater fluxes to the lagoon occurring during periods of relatively
447 constant and high water depths (e.g. from April to October 2017) and high upward
448 advection rates occurring as a consequence of decreases of lagoon water depths (e.g.
449 from July to October 2016). This pattern is consistent with the advection of deep
450 hypersaline porewaters driven by the hydraulic gradient, largely controlled by changes
451 on lagoon water depths: steep hydraulic gradients occur in periods of shallow lagoon
452 water depths or after the rapid drop of lagoon water levels, leading to increased upward
453 advection of porewaters. It should be noted that not only the absolute lagoon water depth
454 but also the rate of change of lagoon water depths are determining the magnitude of
455 porewater fluxes.

456

457 **3.4. Subsurface temperatures and derived enhanced dispersion coefficients**

458 For all locations (Pz1, Pz2, Pz3 and Pz4) and deployment periods (May, June and
459 November), temperature records clearly show large amplitude daily fluctuations in
460 surface waters (typically 3-5 °C) (example in Fig. 9). A damping in the amplitude of
461 diurnal temperature cycles at increasing depths is immediately apparent, as it is the
462 phase shifting with increasing depth of measurement. Separate calibration of the
463 numerical model within the discrete low and high wind (and wave) 48-hour periods was
464 therefore performed to determine whether changes in wave regime induced changes in
465 porewater exchange rate, as reflected by values of the enhanced dispersion coefficient.

466

467 **3.4.1. Estimation of enhanced dispersion coefficients**

468 The enhanced dispersion coefficient (D_e) for each of the selected 48-hour periods is
469 determined by selecting the D_e that best fits (the lowest RMSE) the subsurface
470 temperature records at a given depth. As an example, Fig. 10 shows the variation in RMSE
471 vs D_e for the different 48-hour periods selected in June 2017 (temperatures at 15 cm
472 depth at Pz1). For the two periods of low winds, best-fit values of D_e are $2.6 \cdot 10^{-2} \text{ m}^2 \text{ d}^{-1}$
473 (RMSE values of 0.15 and 0.12 °C, respectively). For the three periods of high wind, best-
474 fit values of D_e are $4.4 \cdot 10^{-2}$, $3.9 \cdot 10^{-2}$ and $3.2 \cdot 10^{-2} \text{ m}^2 \text{ d}^{-1}$ (RMSE values of 0.22, 0.19 and
475 0.02 °C, respectively). Variations in the best-fit RMSE value are probably related partly to
476 the uniformity of the wave conditions (and thus porewater exchanges and D_e) within the
477 chosen 48-hour periods. In many cases, minimum RMSE values are close or lower than
478 the accuracy of the sensors (0.2 °C).

479
480 The best-fit values of D_e for each profile and each of the discrete periods (calm and windy
481 periods) for May and June 2017 deployments, together with their uncertainties, are
482 shown in Table 2. In some cases, modeled temperature could not fit properly the
483 observed temperature (lowest RMSE higher than temperature sensor accuracy) and the
484 D_e values derived from these cases are not reported.

485
486 The approach followed here to estimate dispersion coefficients from temperature time
487 series is based on the assumption that there is no net porewater advection (no advection
488 term in Eq. 4). The relative importance of heat transport by advective to conductive heat
489 flux can be assessed using the dimensionless thermal Peclet Number (P_e) (Anderson,
490 2005; Bhaskar et al., 2012):

491
$$P_e = \frac{vL}{D} \quad (7)$$

492 where v is porewater velocity (m d^{-1}), L is the scale length (m) and D is the dispersion
493 coefficient ($\text{m}^2 \text{d}^{-1}$). Using the maximum vertical porewater fluxes derived from the fluid-
494 salt transport model for the periods of temperature subsurface measurements (v of ~ 5
495 cm d^{-1}), an average value of the estimated enhanced dispersion coefficient under calm
496 conditions ($\sim 0.03 \text{ m}^2 \text{d}^{-1}$) and using the mean grain diameter as the representative length
497 ($L = 2 \cdot 10^{-4} \text{ m}$) as suggested by Bhaskar et al. (2012), gives a thermal Peclet number of
498 $< 10^{-3}$. This value suggests a clear dominance of conductive heat transport over advective
499 transport (Anderson, 2005). A qualitative comparison can also be performed considering
500 the time for surface water temperature changes to propagate to the subsurface. Few
501 hours would be required to propagate the surface temperature signal to the depths at
502 which sensors were installed if heat transport was dominated by dispersion (e.g. ~ 3
503 hours to 15 cm below the sediment-water interface; see Eq. 5), whereas few days would
504 be required if advection was the dominant transport mechanism (~ 3 days). We thus
505 assume that the advective heat transfer will not significantly affect the interpretation of
506 subsurface temperature data.

507
508 It should be noted that both thermal conductivity ($D_{e(\text{cond})}$) and dispersion due to
509 advective porewater exchange ($D_{e(\text{adv})}$) are included within the calculated values of
510 enhanced dispersion coefficient (D_e). The parameters used to estimate $D_{e(\text{cond})}$ following
511 Eq. 6 are summarized in Table 3. Note that none of these parameters are constant, since
512 all of them depend on sediment or water specific properties (e.g. water salinity and
513 temperature, sediment composition, grain size) and they might be highly variable (Duque
514 et al., 2016). Thus, calculated $D_{e(\text{cond})}$ should only be used as an approximation. Estimated
515 $D_{e(\text{cond})}$ range from $1.8 \cdot 10^{-2} \text{ m}^2 \text{d}^{-1}$ at Pz4 ($\theta = 0.70$) to $3.0 \cdot 10^{-2} \text{ m}^2 \text{d}^{-1}$ at Pz3 ($\theta = 0.70$). The
516 enhanced dispersion coefficients (D_e) derived from temperature profiles for the calm

517 periods in May and June 2017 are in general good agreement with the theoretically
518 calculated thermal conductivities ($D_{e(cond)}$ in Eq. 6), particularly for the stations Pz1, Pz2
519 and Pz3 (Fig. 11). This suggests that the porewater temperature records for calm periods
520 are mainly governed by thermal conductivity. Notice that there is a significant
521 disagreement between the calculated thermal conductivity and the estimated D_e for calm
522 periods for Pz4, but these differences could be related to the used of literature-based
523 thermal parameters instead of specific measurements for the clayey sediments of Pz4.

524

525 **3.4.2. Comparison of dispersion coefficients for calm and windy conditions**

526 As shown in Table 2 and Fig. 11, enhanced dispersion coefficients (D_e) obtained for windy
527 48-hour periods for a given location are generally higher than those obtained for calm
528 periods. A Kruskal-Wallis test was applied to compare modeled enhanced dispersion
529 coefficients for windy and calm periods (evaluating together the results from the 10 cm
530 and 15 cm sensors for the different deployments), confirming that modeled D_e for windy
531 periods are significantly higher than those modeled for calm periods for the deployments
532 of May and June 2017 (Kruskal-Wallis, $p < 0.01$).

533

534 When the results are clustered by locations, D_e for windy periods are consistently higher
535 than those modeled for calm periods in all the stations (Fig. 11). The difference in D_e at
536 each site between calm and windy periods reveals an increase of the rate of heat
537 transport in windy periods, likely driven by enhanced porewater exchange fluxes.

538 Assuming that the modeled D_e for the calm periods represents mainly heat transport due
539 to thermal conductivity, the effective dispersion driven by porewater exchange ($D_{e(adv)}$)
540 can be estimated as the difference between D_e in calm and windy periods. Estimated
541 $D_{e(adv)}$ during the wind periods for 15 cm temperature sensors are $(1.7 \pm 0.6) \cdot 10^{-2}$, $(2.5 \pm$

542 $0.8) \cdot 10^{-2}$, $(1.4 \pm 0.7) \cdot 10^{-2}$ and $(0.6 \pm 0.6) \cdot 10^{-2} \text{ m}^2 \text{ d}^{-1}$ for stations Pz1, Pz2, Pz3 and Pz4 in
543 May 2017, respectively, and $(1.2 \pm 0.6) \cdot 10^{-2}$, $(1.0 \pm 1.1) \cdot 10^{-2}$, $(1.5 \pm 1.2) \cdot 10^{-2}$ and $(0.4 \pm$
544 $0.4) \cdot 10^{-2} \text{ m}^2 \text{ d}^{-1}$ for stations Pz1, Pz2, Pz3 and Pz4 in June 2017. Slightly lower but
545 comparable coefficients are estimated when using the temperature sensors installed at
546 10 cm below the sediment-water interface. The only station where dispersion driven by
547 porewater fluxes (i.e. differences in D_e modeled for calm and windy periods) is not
548 statistically significant is Pz4, where the presence of low-permeability sediments
549 (permeabilities $< 10^{-12} \text{ m}^2$) likely results in a significant reduction of porewater fluxes
550 (Huettel et al., 2014).

551 **4. DISCUSSION**

552 **4.1. Deep porewater fluxes to La Palme lagoon driven by oscillations of lagoon**
553 **water depths: insights from porewater salinities**

554 The hydraulic gradient between the aquifer and coastal water bodies (and its seasonal
555 variations) is commonly a major force driving groundwater or porewater fluxes (Santos
556 et al., 2012). Many studies have focused on the influence and variability of inland
557 groundwater head, which is driven by the aquifer recharge (Anderson and Emanuel,
558 2010; Michael et al., 2005; Sugimoto et al., 2015; Yu et al., 2017), and only a limited
559 number of studies have evaluated how changes on surface water levels in receiving water
560 bodies alter the hydraulic gradient and, consequently, the water and solute fluxes across
561 the land-ocean interface (Gonneea et al., 2013; Lee et al., 2013; Michael et al., 2013).

562
563 In the case of La Palme Lagoon, water depths in the lagoon are controlled by both i)
564 seasonal changes on the balance between water inputs and evaporative losses (e.g. higher
565 evaporation and lower water inputs in dry summer months, resulting in lower water
566 levels in summer), and ii) wind events that control the opening of the sandy barrier and
567 the exchange of water between the lagoon and the open sea. Changes on lagoon water
568 depths are thus occurring over relatively short time-scales (few days-weeks), when the
569 inland hydraulic head can be assumed to be constant. Maximum variations in coastal
570 piezometric levels from the alluvial aquifer are indeed on the order of 30-40 cm
571 (piezometer code BSS002LRH; ades.eaufrance.fr), occurring over annual cycles. In
572 addition, the relatively large size of the lagoon limits the effect of variations in inland
573 groundwater head on porewater fluxes. Lagoon water depth is thus expected to
574 contribute more to the variability in the hydraulic gradient than variation in groundwater
575 head does. As a consequence, in periods of decreases of lagoon water depths, the

576 increased hydraulic gradient favors the upward advection of deep hypersaline
577 porewaters (porewater fluxes up to 25 cm d⁻¹), as derived from the results of the fluid-
578 salt transport model and the measured subsurface salinities (Fig. 8). Similarly, increases
579 of lagoon water depths may force the infiltration of lagoon waters into the sediments
580 driven by the reduced hydraulic gradient and density convection.

581

582 **4.2. Shallow porewater fluxes to La Palme lagoon driven by wind waves: insights** 583 **from temperature time series**

584 **4.2.1. Drivers of increased heat transport during windy periods**

585 A number of driving forces have been identified to produce transient porewater fluxes
586 across the sediment-water interface, including hydraulic gradients, wave and tidal
587 pumping, interaction of bottom currents and seafloor topography, density instabilities
588 and pumping activities of benthic fauna (Huettel et al., 2014; Santos et al., 2012).

589 Among all the potential drivers, short-term wind-driven wave forcing is the only
590 mechanism that can explain the highly dynamic nature of the observed porewater fluxes
591 with systematically higher fluxes during windy periods. As detailed in section 3.2, the
592 strong SE and, mainly, NW winds in the area produce locally-generated wind waves that
593 can reach significant wave heights of 5-10 cm lasting for some hours to few days.

594

595 Wave action can drive large volume of water to circulate under the swash zone, but this
596 mechanism is only acting in the shoreline (Li and Barry, 2000; Robinson et al., 2014; Sous
597 et al., 2016). In submerged areas, waves can also induce advective shallow porewater
598 exchange fluxes either through pressure gradients generated by the different hydrostatic
599 pressures between wave crests and troughs or through wave-induced oscillatory
600 currents that interact with sediment topography (Cardenas and Jiang, 2011; Li et al.,

601 2017; Precht and Huettel, 2003). Wind-driven waves and currents can also induce shear
602 stress producing resuspension of sediments and increasing the magnitude of porewater
603 exchange fluxes (Almroth-Rosell et al., 2012; Whipple et al., 2018). The magnitude of
604 wind- (wave-) driven porewater fluxes will depend on both the physical characteristics of
605 the water body (e.g. hydraulic conductivities of the sediments, water depths) and the
606 magnitude of the forcing itself (i.e. wave frequency, wave amplitude, duration of the
607 events) (Robinson et al., 2017).

608
609 Qian et al (Qian et al., 2009) developed a model to examine the effect of wave action on
610 porewater solute profiles, which related the enhanced dispersion coefficient at the
611 sediment surface with wave and sediment parameters:

$$612 \quad D_e = \frac{5\alpha K a}{L\theta} \quad (8)$$

613 where α is the hydrodynamic dispersivity (m), K is the sediment hydraulic conductivity
614 (m d^{-1}), a is the half-wave amplitude and L is the wavelength (m). Using previously
615 derived parameters for La Palme lagoon ($\alpha = 0.005$ m; $L = 1$ m; $K = 2\text{-}4$ m d^{-1} ; (Cook et al.,
616 2018a)) and $a = 0.03\text{-}0.05$ m derived from wave measurements, a D_e at the sediment-
617 water interface of $(0.4 - 1.3) \cdot 10^{-2} \text{ m}^2 \text{ d}^{-1}$ is calculated. This range is comparable with the
618 modeled thermal dispersion driven by porewater fluxes ($D_{e(adv)}$), suggesting that the
619 increase in porewater flux in windy (wave) periods is consistent with wave pumping
620 being the principal driver of porewater fluxes in La Palme lagoon.

621

622 **4.2.2. Magnitude of wave-driven shallow porewater fluxes**

623 Estimating the porewater flux required to create these modeled $D_{e(adv)}$ is not a
624 straightforward step (Rau et al., 2014). For solute transport (as opposed to heat

625 transport), the dispersion coefficient (D_e) can be related to porewater flux through the
626 hydrodynamic dispersivity (α)

$$627 \quad D_e = \frac{2\bar{q}_v\alpha}{\theta} \quad (9)$$

628 where \bar{q}_v is the mean upward or downward flux averaged across the upwelling and
629 downwelling phases (Anderson, 2005; Cook et al., 2018a). The calculated \bar{q}_v is thus a
630 function of the selected hydrodynamic dispersivity (α), which is a scale-dependent
631 parameter difficult to constrain for short-scale porewater fluxes (Cook et al., 2018a).
632 Whereas solute dispersion depends linearly on fluid velocity, the linear dependence of
633 thermal dispersion and fluid velocity is under debate (Bhaskar et al., 2012; Molina-
634 Giraldo et al., 2011; Rau et al., 2012). Assuming that the dispersion of heat is analogous to
635 dispersion of a conservatively transported solute tracer in water, calculated median
636 porewater exchange rates during windy periods would be on the order of 50 cm d⁻¹
637 (derived from Eq. 9, using a hydrodynamic dispersivity of 0.005 m (Cook et al., 2018a;
638 Gelhar et al., 1992)). Considering that the average water depths of La Palme lagoon
639 usually ranges from 0.5 to 1.5 m, the porewater exchange rates estimated in this study
640 would imply that the entire water volume of the lagoon would circulate through its
641 sediments every 1 - 3 days, i.e. during a multi-day wind event.

642
643 King et al. (King et al., 2009) used a generalized analytical model to estimate wave-driven
644 porewater rates on the order of 10 cm d⁻¹ for a setting with characteristics similar to
645 those from La Palme lagoon (wave amplitude of 5 cm; wave period of 1 s; water depth of
646 0.5 m; permeability of 10¹¹ m²). Even though these estimates from King et al. (2009) do
647 not consider the porewater fluxes caused by the interaction of oscillatory flows and
648 bottom topography, which may exceed those fluxes from wave pumping alone (Precht
649 and Huettel, 2003), these rates are comparable with the advection rates roughly

650 estimated for wind periods in La Palme lagoon. Thus, temperature-derived porewater
651 fluxes estimated for strong wind events in La Palme lagoon are likely a good order-of-
652 magnitude approximation of wave-driven porewater fluxes for the studied site.

653

654 **4.3. Magnitudes and temporal scales of driving forces and porewater fluxes**

655 Recent studies conducted in La Palme lagoon have estimated average porewater fluxes to
656 the entire lagoon to be on the order of 0.8 – 4.1 cm d⁻¹ (Bejannin et al., 2017; Rodellas et
657 al., 2018; Stieglitz et al., 2013; Tamborski et al., 2018). These fluxes, which were
658 estimated from whole-of-lagoon radionuclide mass balances, are in good agreement with
659 the porewater fluxes driven by oscillations of lagoon water depths estimated in this study
660 from the fluid-salt transport model (yearly averaged porewater fluxes of 1.2 cm d⁻¹;
661 interquartile range (q1 – q3) of -3.0 – 3.2 cm d⁻¹). Some of the whole-of-lagoon studies
662 were conducted in calm periods with relatively high and constant lagoon waters depths
663 (e.g. April and June 2017; (Rodellas et al., 2018)), when porewater fluxes driven by
664 oscillations of lagoon water depths and wind-driven waves are expected to be low as
665 inferred from subsurface salinities and temperatures. We thus cannot exclude the
666 existence of a porewater base flux to La Palme lagoon driven by other mechanisms (e.g.
667 bioirrigation, current-topography interactions, etc.). However, results of this study
668 provide evidence that porewater fluxes increase significantly during periods of decreases
669 of lagoon water depths or during strong wind events, as a consequence of increased
670 hydraulic gradients and increased wave pumping, respectively (Fig. 12).

671

672 Importantly, the two mechanisms evaluated in this study occur over different spatial and
673 temporal scales. At the larger scale, variations of the lagoon water depth drive deep
674 porewater fluxes at the scale of meters. At the smaller scale, wind-driven waves force

675 surface water to move in and out of the shallow sediments (i.e. shallow porewater fluxes).
676 The length of the porewater flowpath have a large influence on the biogeochemical
677 processes occurring within sediments and on the chemical composition of porewaters
678 discharging across the sediment-water interface (Heiss et al., 2017; Lamontagne et al.,
679 2018; Weinstein et al., 2011). Consequently, the spatial scale of porewater fluxes needs to
680 be considered to evaluate the overall magnitude of solute inputs driven by porewater
681 fluxes. From a temporal perspective, porewater fluxes driven by wave pumping will only
682 occur during important wind events, typically over periods of 1-3 days (Fig. 4).
683 Contrarily, reduced lagoon water depths occur mainly as a consequence of the high
684 evaporative loss in summer and/or strong wind events that control the opening of the
685 sandy barrier and force the export of water towards the Mediterranean Sea. Periods of
686 shallow water depths are typically extending from several days to few months (Fig. 3.b)
687 and thus the duration of porewater fluxes forced by reduced lagoon water depths can be
688 far larger than that of wave-induced fluxes.

689

690 A proper evaluation of the magnitude of porewater fluxes and their relevance for water
691 systems thus requires understanding their temporal and spatial scales. As detailed in
692 Wilson et al. (2015), most of the studies conducted elsewhere evaluating porewater
693 fluxes are focused on specific short-term (1-5 days) samplings that only provide “snap-
694 shot” observations and that are generally biased towards the summer field season and
695 periods with calm conditions, when some of the driving forces (e.g. wind-waves) might
696 not operate. Long-term observations are thus required to capture all the potential
697 mechanisms driving porewater fluxes, including those forcings operating in sporadic
698 intense events (e.g. storms, heavy rainfalls) (Sawyer et al., 2013; Smith et al., 2008). In
699 addition, the driving force that is captured will also depend on the tracer technique or

700 approach used to estimate porewater fluxes (Cook et al., 2018b; King, 2012; Rodellas et
701 al., 2017). Future studies in lagoons and coastal environments should focus on long-term
702 observations and combine different tracers to capture and differentiate the fluxes
703 produced by the diverse driving mechanisms. Long-term studies also allow isolating the
704 driving mechanism based on temporal variations of porewater fluxes, considering
705 periods when one forcing dominates over the other (Cook et al., 2018b), as done in this
706 study. It should additionally be noted that the interaction between different forcings is
707 generally nonlinear and porewater fluxes cannot be estimated simply as a sum of
708 independent drivers (King, 2012; Yu et al., 2017). Rather, a thorough understanding of
709 the different drivers and their interactions is required.

710

711 **CONCLUSIONS**

712 This study documents the role of lagoon water depth variations and wind-driven waves
713 as drivers of porewater fluxes in a coastal lagoon. The dynamics of these physical driving
714 forces are evaluated in isolation, through measurements of variations of salinity and
715 temperature in the subsurface:

- 716 - The temporal and vertical variability of porewater salinity profiles (coupled with a
717 fluid and salt transport model) suggests that oscillations of lagoon water depth act as
718 a major control on the fluxes of deep (>1 m) porewaters. In periods of shallow lagoon
719 water depths or when sudden decreases of lagoon water depths occur, the increased
720 hydraulic gradient favors the upward advection of deep hypersaline porewaters,
721 whereas porewater inputs are restricted (or reversed) in periods of constant and
722 high lagoon water depths.
- 723 - The temperature records in the lagoon subsurface (coupled with a heat transport
724 model) reveal that porewater fluxes are significantly higher in windy periods as a

725 consequence of locally-generated wind waves that force the circulation of lagoon
726 waters through sediments.

727
728 Wave pumping and the hydraulic gradient contribute to significantly increase porewater
729 fluxes to the lagoon during wind events and in periods with shallow lagoon water depths,
730 respectively. Whereas the large fluxes driven by wave pumping only flush relatively
731 shallow sediments and are restricted to the duration of strong wind events, porewater
732 fluxes driven by the hydraulic gradient involve deeper sediments (> 1 m) and their
733 relevance may extend for longer periods (up to few months). The temporal and spatial
734 scale of porewater fluxes will largely determine the overall magnitude of solute inputs
735 driven by porewater fluxes. An appropriate evaluation of not only the magnitude of
736 porewater fluxes but also their underlying physical forces is thus required to fully
737 understand the significance of these fluxes and their implications for coastal water
738 bodies.

739

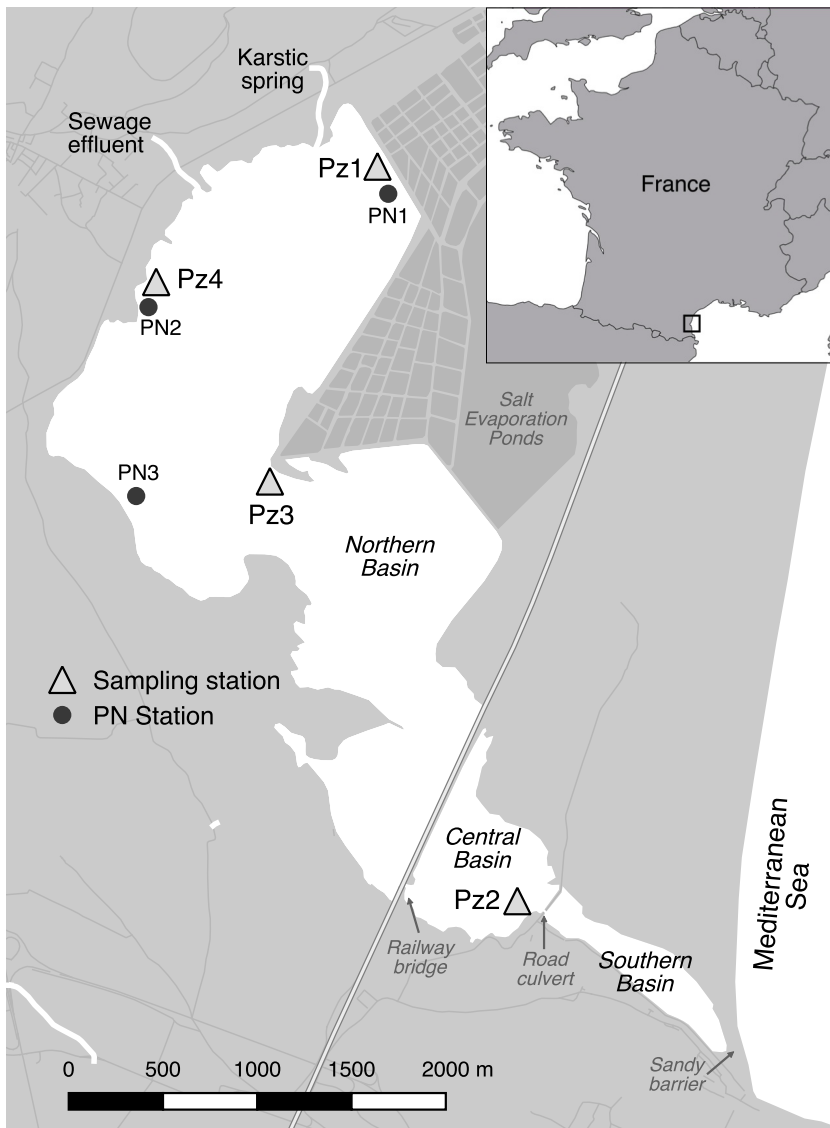
740 **Acknowledgements**

741 This research is a contribution to the ANR @RAction chair (ANR-14-ACHN-0007-01 – T
742 Stieglitz) and Labex OT-Med (ANR-11-LABEX-0061, part of the “Investissements
743 d’Avenir” program through the A*MIDEX project ANR-11-IDEX-0001-02) funded by the
744 French National Research Agency (ANR). This project has received funding from the
745 European Union’s Horizon 2020 research and innovation programme under the Marie
746 Skłodowska-Curie grant agreement No 748896. V. R. acknowledges financial support
747 from the Beatriu de Pinós postdoctoral programme of the Catalan Government (2017-BP-
748 00334) P.G. Cook acknowledges support from IméRA (Institute of Advanced Studies), Aix-
749 Marseille Université (Labex RFIEA and ANR “Investissements d’avenir”). We thank C

750 Fleger and K Fortune from the “Parc Naturel Régional de la Narbonnaise en
751 Méditerranée” (PNRNM; France), M David (IFREMER, BRGM, CEREGE; France), V Bailly-
752 Comte (BRGM), P Dussouillez and J Fleury (CEREGE) for their help in sampling field trips
753 and experimentation, as well as Wilson and C George (University of South Carolina; USA)
754 for their recommendations on heat transport modeling. We thank A. Calafat and M. Guart
755 (Universitat de Barcelona) for the analysis of sediment grain size distribution. We are
756 also grateful to *GLADYS* research group (www.gladys-littoral.org) who supported the
757 experimentation.
758

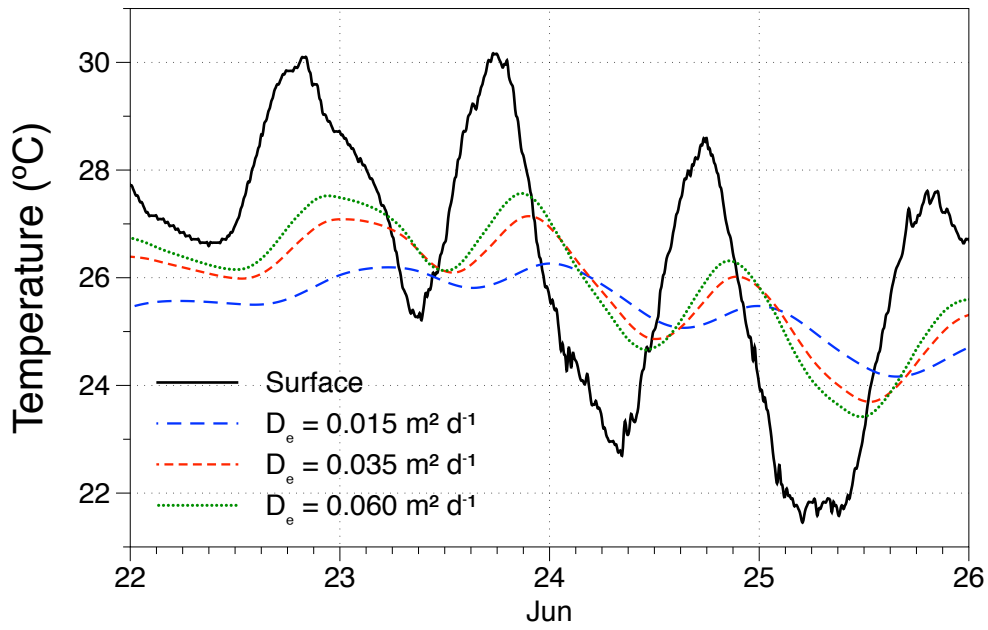
759 **FIGURES**

760 **FIGURE 1**



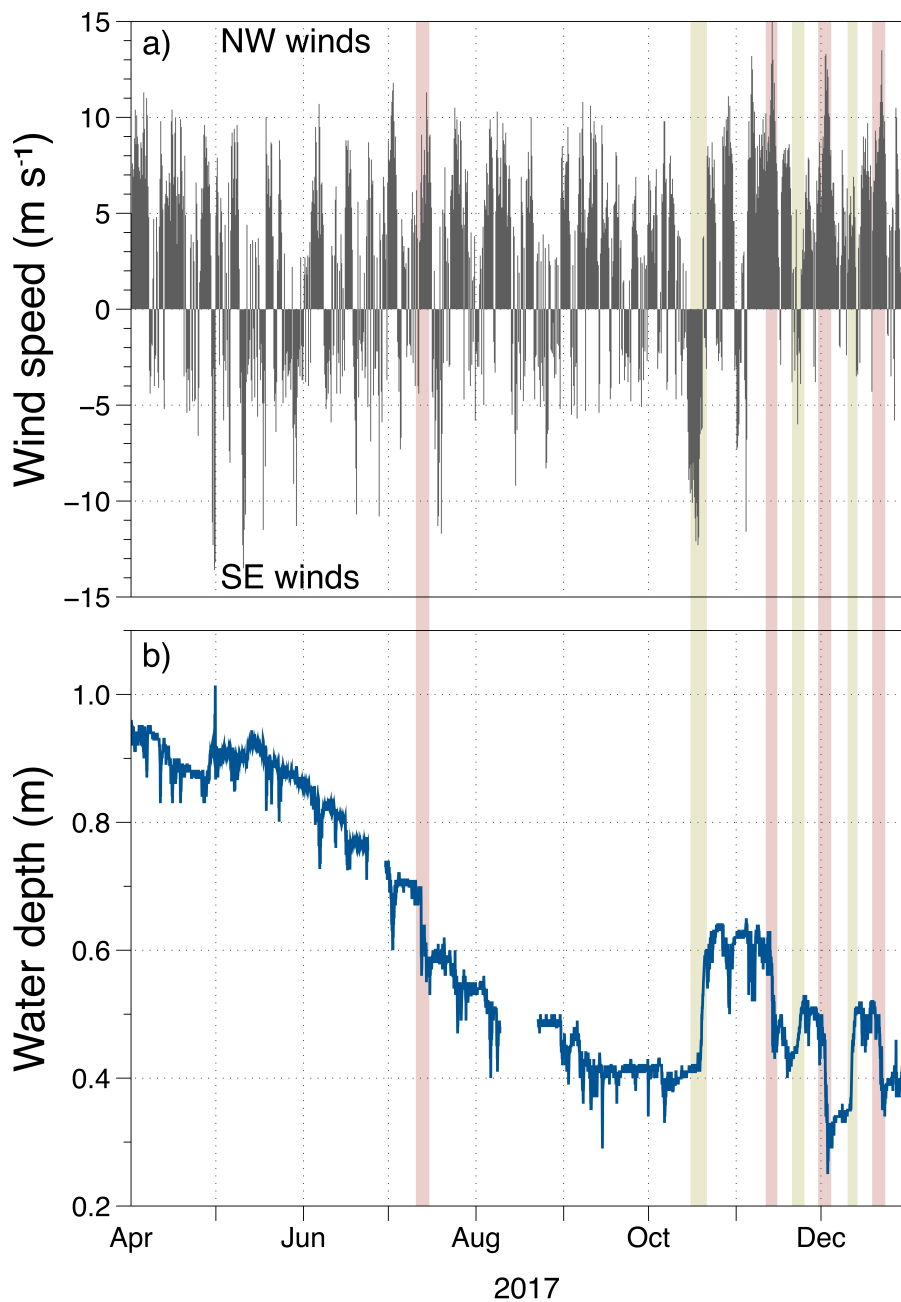
761
762 **Figure 1.** Study site (La Palme lagoon) location on the French Mediterranean coastline.
763 The location of sampling stations (Pz1, Pz2, Pz3 and Pz4) for sediment core collection,
764 temperature and CTD logger installation and porewater collection are shown. The
765 position of monitoring stations (PN1, PN2 and PN3) from the “Parc Naturel Régional de la
766 Narbonnaise en Méditerranée” (PNRNM) is also indicated.
767

768 **FIGURE 2**



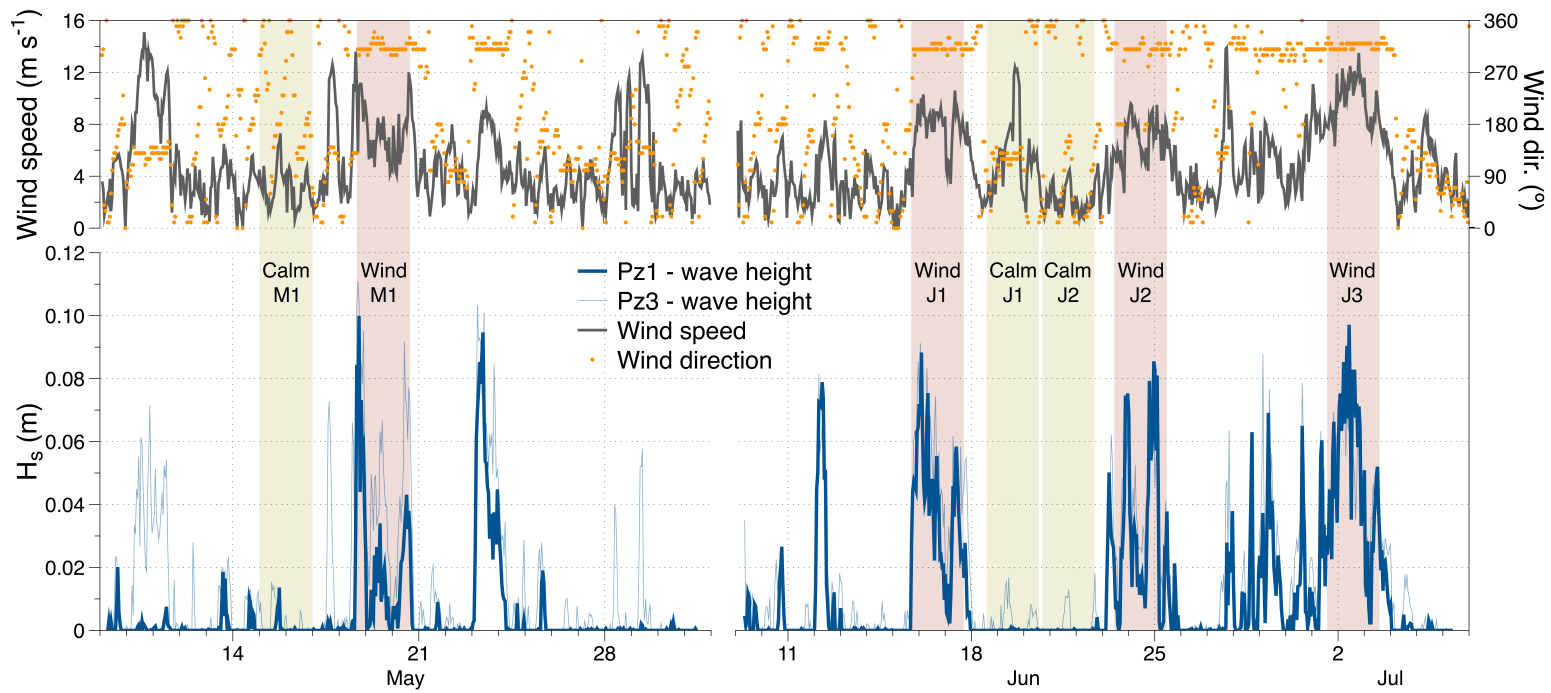
769
770 **Figure 2.** Measured surface water temperatures at Pz1 between 22-26 June 2017, and
771 modeled subsurface temperatures at 15 cm depth based on enhanced dispersion
772 coefficients (D_e) between $1.5 \cdot 10^{-2}$ and $6.0 \cdot 10^{-2} \text{ m}^2 \text{ d}^{-1}$.

773



775
 776 **Figure 3.** a) Wind speeds (averaged for 6 hours) and b) water depth variations in Pz1
 777 during the main period of samplings (April 2017 – December 2017). For simplicity, all the
 778 winds blowing from the N ($270^{\circ} - 90^{\circ}$) are represented as positive and assumed to be
 779 NW winds, and winds blowing from the S ($90^{\circ} - 270^{\circ}$) are represented as negative and
 780 assumed to be SE winds. Green and red vertical areas highlight abrupt increase or
 781 decrease, respectively, in lagoon water depths.

782 **FIGURE 4**

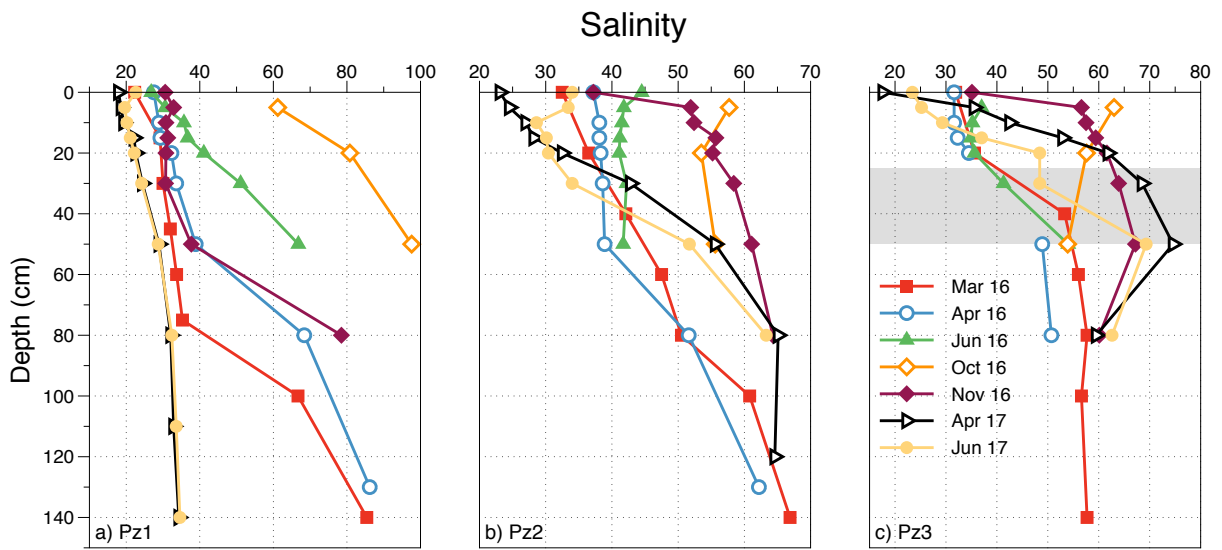


784 **Figure 4.** Significant wave height H_s (m) measured at stations Pz1, Pz2 and Pz3 during
 785 the three periods of deployment of temperature sensors and high-frequency pressure
 786 sensors. Hourly-averaged wind speeds (m s^{-1}) and directions ($^\circ$) are also shown. Discrete
 787 48-hour periods selected to represent both high (red vertical areas) and low (green
 788 vertical areas) wave conditions are also shown.

789

790

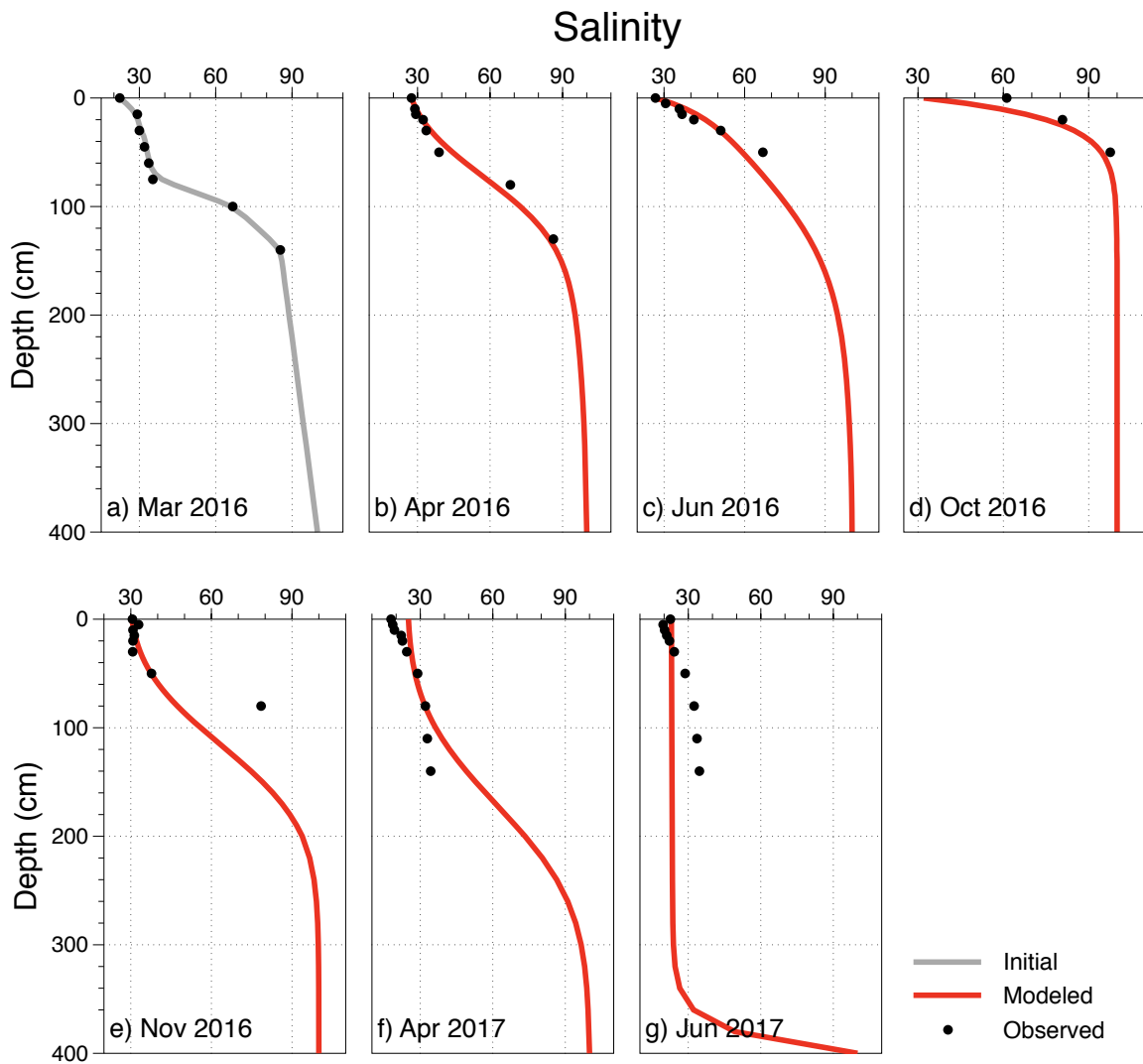
791 **FIGURE 5**



792

793 **Figure 5.** Depth profiles (in cm below the sediment-water interface) of salinity in
794 porewater for the three piezometers collected at each campaign. Reported values at a
795 depth of 0 correspond to the samples collected in surface waters (~10 cm above the
796 sediment-water interface). The grey area represents the position of the layer with low
797 permeability found at Pz3.

798



800

801 **Figure 6.** Observed and modeled porewater salinity profiles (depth in cm below the

802 sediment-water interface) at station Pz1 from the different sampling campaigns. The grey

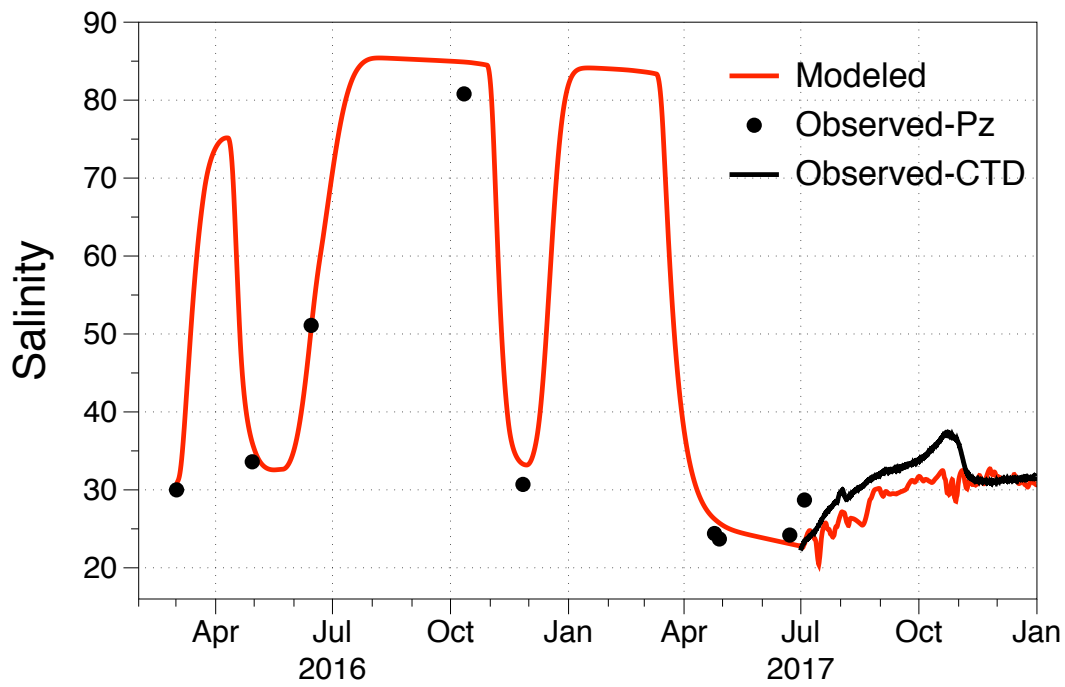
803 salinity profile shown in (a) represents the linear interpolation between the measured

804 salinities in March 2016 and the lower boundary conditions, which is used as initial

805 concentration profile for the model.

806

807 **FIGURE 7**



808

809 **Figure 7.** Observed and modeled salinities at 30 cm below the sediment-water interface

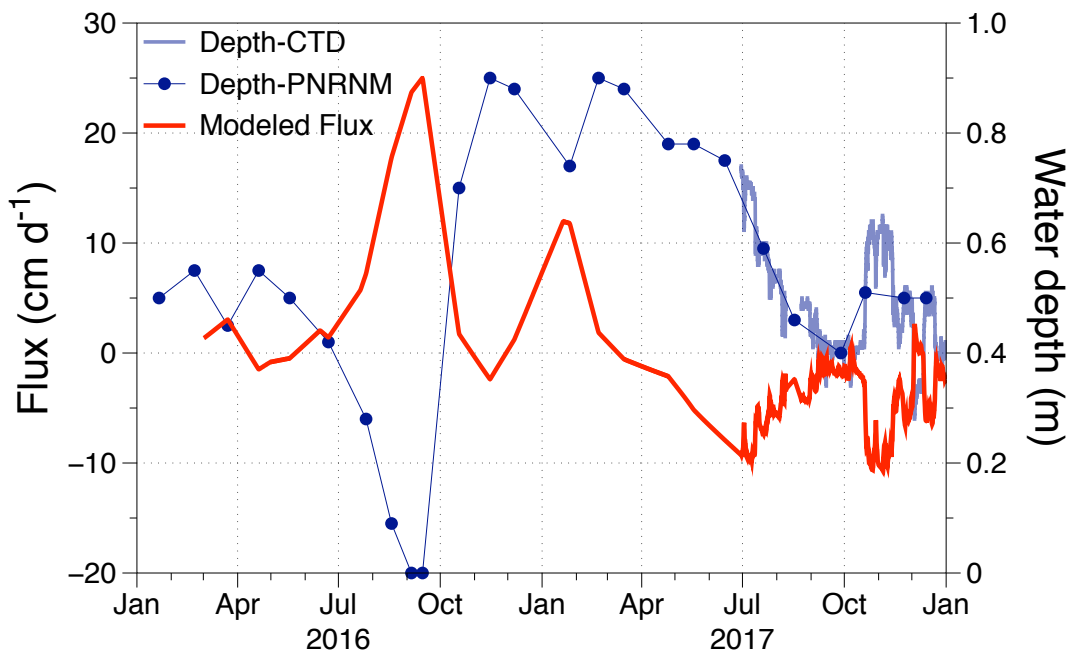
810 at station Pz1 for the studied period (2016-17). Observed data include porewater

811 samples collected with piezometers (“Observed-Pz”) and directly measured with the CTD

812 logger installed in the sediments (“Observed-CTD”).

813

814 **FIGURE 8**



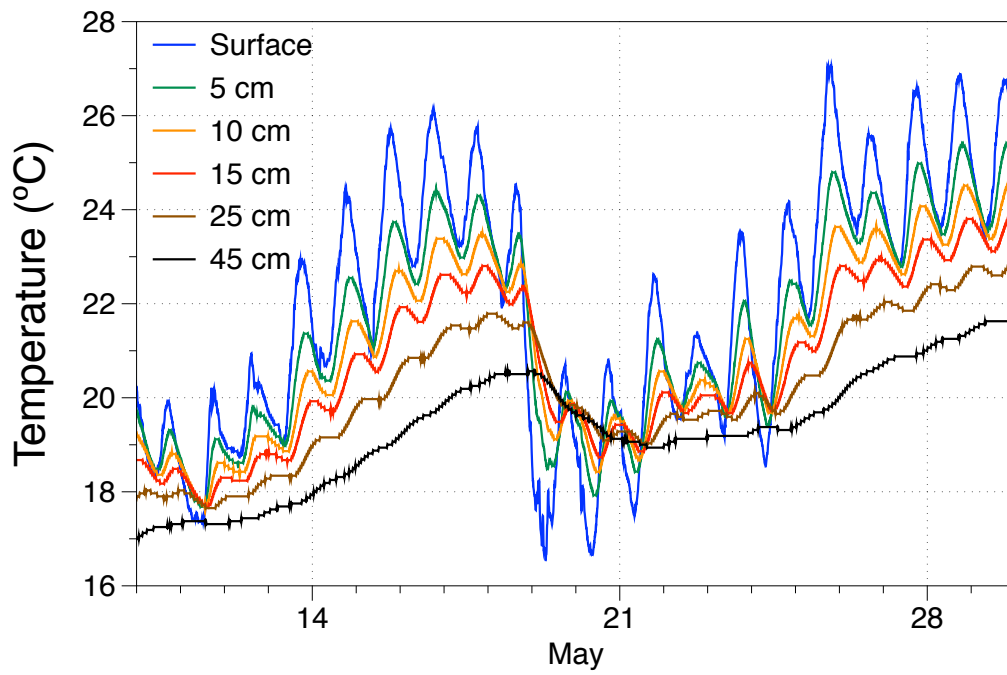
815

816

817 **Figure 8.** Modeled vertical porewater fluxes (cm d⁻¹) at station Pz1, together with
818 variations of lagoon water depths at the same station (including monthly measurements
819 from PNRNM and continuous measurements with the CTD logger installed at surface
820 waters). Positive porewater fluxes represent advection from sediments to surface lagoon
821 waters.

822

823 **FIGURE 9**

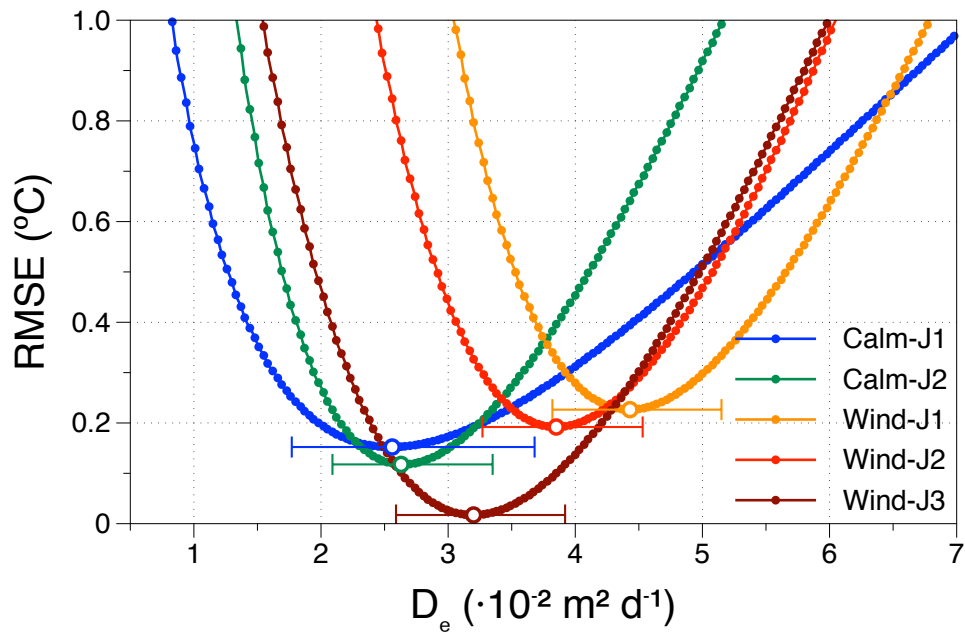


824

825 **Figure 9.** Temperature records at station Pz1 for the May 2017 deployment period,
826 including temperatures in surface waters and at different depths below the sediment-
827 water interface.

828

829 **FIGURE 10**



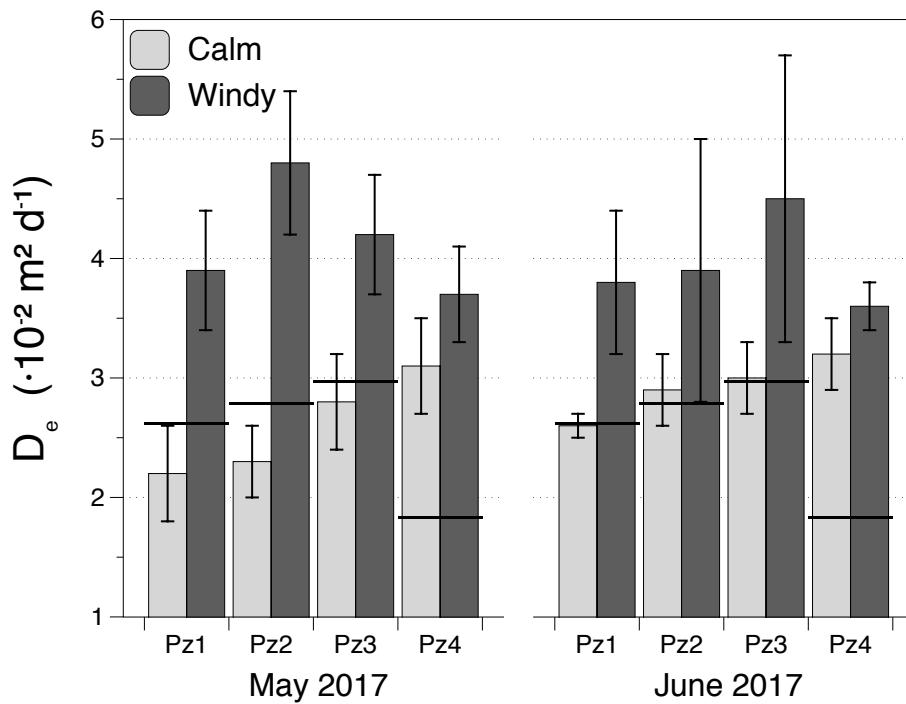
830

831 **Figure 10.** Dispersion coefficient (D_e) versus RMSE for June 2017 data for the
832 temperature sensor at 15 cm depth at Pz1. The different D_e vs RMSE curves account for
833 the different discrete 48-hours periods selected for June 2017 temperature data (Fig. 4):
834 2 calm periods (Calm-J1 and Calm-J2) and 3 windy periods (Wind-J1, Wind-J2 and Wind-
835 J3). Minimum values of RMSE for each period indicate the best-fit value of D_e .

836 Uncertainties are defined by RMSE values 0.1 °C greater than the minimum RMSE in each
837 case.

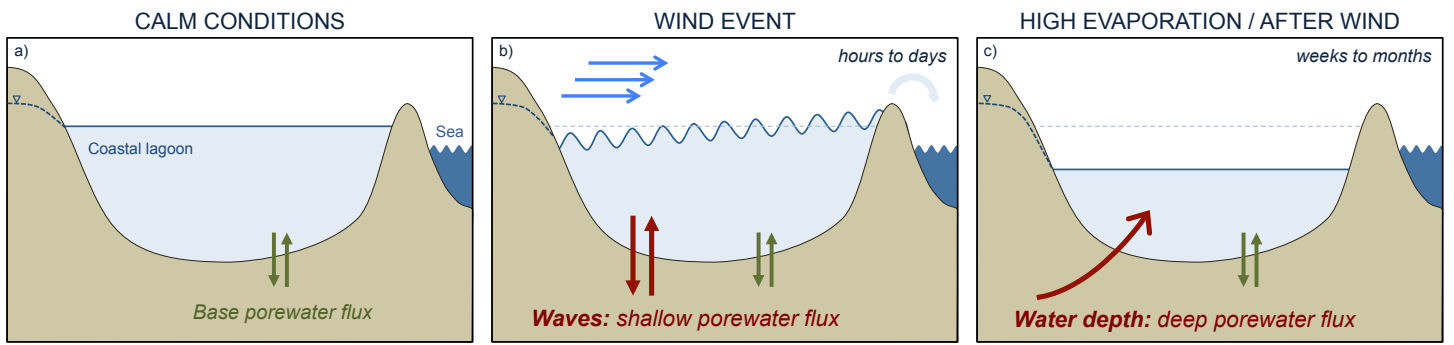
838

839 **FIGURE 11**



840
 841 **Figure 11.** Best-fit values of enhanced dispersion coefficients (D_e) for 15 cm temperature
 842 sensors derived from the 48-hour periods from May and June 2017 deployments. D_e
 843 reported for June 2017 represent the average (\pm standard deviation) of the 2 (calm) or 3
 844 (windy) events selected during this deployment. Horizontal black lines represent the
 845 thermal conductivity estimated from Eq. 6.
 846

847 **FIGURE 12**



849

850 **Figure 12.** Conceptual model describing changes on shallow and deep porewater fluxes

851 into a coastal lagoon depending on variations of lagoon water depths and locally-

852 generated wind waves: a) Potential base porewater flux in periods of calm, high water

853 conditions; b) Locally-generated wind waves produce an increase of shallow porewater

854 fluxes; c) The reduced lagoon water depths (as a consequence of high evaporation or the

855 wind-driven outflow of lagoon waters) produce an increase of deep porewater fluxes.

856

857 .

858 **TABLES**

859 **TABLE 1**

860 **Table 1.** Parameter values used in the one-dimensional model of subsurface salinities.

861 Values for h represent the pressure head, not the total head.

862

Parameter	Units	Specified value	Allowable range	Calibrated value
h_{top}	m	0 - 0.91*	-	-
h_{bot}	m	-	3.0 - 5.0	Day 0: 4.32 Day 182: 4.24 Day 365: 4.80 Day 547: 4.17 Day 730: 4.13
C_{top}	-	16.8 - 35.9 *	-	-
C_{bot}	-	-	90 - 130	100
k	m^2	-	10^{-13} - 10^{-12}	$1.63 \cdot 10^{-12}$ **
μ	$Pa\ s$	$8.9 \cdot 10^{-4}$	-	-
$\partial\rho/\partial C$	-	0.77	-	-
θ	-	-	0.4 - 0.5	0.40
S_{op}	Pa^{-1}	$1 \cdot 10^{-8}$	-	-
α	m	-	0.2 - 1.0	0.2
D_M	$m^2\ s^{-1}$	$1.16 \cdot 10^{-9}$	-	-

863

864 * Taken from measurements in the Lagoon (at stations Pz1 and PN1).

865 ** Corresponds to a hydraulic conductivity of $1.55\ m\ d^{-1}$ for non-saline water.

866

867

868

869

870

871 **TABLE 2**

872 **Table 2.** Best-fit values of enhanced dispersion coefficients for 0.10 and 0.15 m
 873 temperature sensors for discrete 48-hour periods. Units are $\cdot 10^{-2} \text{ m}^2 \text{ d}^{-1}$. No simulations
 874 were conducted for loggers at stations Pz2 and Pz4 in November 2017 because water
 875 depths were too shallow and the surface sensor was often outside the water. n.r. indicates
 876 cases when the data from the logger could not be recovered.

877

Event Numb	Pz	Sensor at 10 cm			Sensor at 15 cm		
		Best_10cm	$-\Delta$	$+\Delta$	Best-15cm	$-\Delta$	$+\Delta$
May 17							
Calm-M1	PZ1	2.3	0.4	0.5	2.2	0.4	0.4
Calm-M1	PZ2	3.0	0.5	0.6	2.3	0.3	0.4
Calm-M1	PZ3	2.8	0.4	0.5	2.8	0.4	0.4
Calm-M1	PZ4	3.1	0.5	0.5	3.1	0.4	0.4
Wind-M1	PZ1	3.3	0.4	0.5	3.9	0.5	0.5
Wind-M1	PZ2	4.0	0.5	0.6	4.8	0.6	0.8
Wind-M1	PZ3	3.8	0.5	0.6	4.2	0.5	0.6
Wind-M1	PZ4	3.3	0.4	0.5	3.7	0.4	0.5
June 17							
Calm-J1	PZ1	n.r.			2.6	0.8	1.1
Calm-J2	PZ1	n.r.			2.6	0.5	0.7
Calm-J1	PZ2	2.7	0.5	0.5	3.1	0.5	0.6
Calm-J2	PZ2	2.5	0.4	0.4	2.7	0.4	0.4
Calm-J1	PZ3	2.5	0.6	0.7	3.2	0.6	0.8
Calm-J2	PZ3	2.4	0.4	0.4	2.8	0.4	0.4
Calm-J1	PZ4	n.r.			3.4	0.5	0.6
Calm-J2	PZ4	n.r.			3.0	0.4	0.5
Wind-J1	PZ1	n.r.			4.4	0.6	0.7
Wind-J2	PZ1	n.r.			3.9	0.6	0.7
Wind-J3	PZ1	n.r.			3.2	0.6	0.7
Wind-J1	PZ2	4.0	0.5	0.6	4.8	0.6	0.8
Wind-J2	PZ2	3.4	0.5	0.6	4.0	0.6	0.8
Wind-J3	PZ2	2.6	0.6	0.7	2.7	0.6	0.8
Wind-J1	PZ3	4.1	0.6	0.8	5.4	0.9	1.1
Wind-J2	PZ3	3.9	0.6	0.7	4.9	0.8	0.9
Wind-J3	PZ3	2.6	0.6	0.8	3.1	0.7	0.9
Wind-J1	PZ4	n.r.			3.8	0.5	0.7
Wind-J2	PZ4	n.r.			3.6	0.5	0.6
Wind-J3	PZ4	n.r.			3.3	0.6	0.7

878

879 **TABLE 3**

880 **Table 3.** Parameters used for deriving thermal conductivity (Irvine et al., 2015; Wilson et
881 al., 2016).

Parameter	Symbol	Value	Units
Density of water	ρ_w	1025	kg m ⁻³
Density of solids	ρ_s	2650	kg m ⁻³
Specific heat capacity of water	c_w	4180	J kg ⁻¹ °C ⁻¹
Specific heat capacity of solids	c_s	1170	J kg ⁻¹ °C ⁻¹
Thermal conductivity of water	K_w	0.57	J s ⁻¹ m ⁻¹ °C ⁻¹
Thermal conductivity of solids	K_s	2.0	J s ⁻¹ m ⁻¹ °C ⁻¹

882

883 **REFERENCES**

- 884 Almroth-Rosell, E., Tengberg, A., Andersson, S., Apler, A., Hall, P.O.J., 2012. Effects of
885 simulated natural and massive resuspension on benthic oxygen, nutrient and
886 dissolved inorganic carbon fluxes in Loch Creran, Scotland. *J. Sea Res.* 72, 38–48.
887 <https://doi.org/10.1016/J.SEARES.2012.04.012>
- 888 Anderson, M.P., 2005. Heat as a Ground Water Tracer. *Ground Water* 43, 951–968.
889 <https://doi.org/10.1111/j.1745-6584.2005.00052.x>
- 890 Anderson, W.P., Emanuel, R.E., 2010. Effect of interannual climate oscillations on rates of
891 submarine groundwater discharge. *Water Resour. Res.* 46.
892 <https://doi.org/10.1029/2009WR008212>
- 893 Andrisoa, A., Stieglitz, T.C., Rodellas, V., Raimbault, P., 2019. Primary production in coastal
894 lagoons supported by groundwater discharge and porewater fluxes inferred from
895 nitrogen and carbon isotope signatures. *Mar. Chem.* 210, 48–60.
896 <https://doi.org/10.1016/J.MARCHEM.2019.03.003>
- 897 Anschutz, P., Smith, T., Mouret, A., Deborde, J., Bujan, S., Poirier, D., Lecroart, P., 2009.
898 Tidal sands as biogeochemical reactors. *Estuar. Coast. Shelf Sci.* 84, 84–90.
899 <https://doi.org/10.1016/j.ecss.2009.06.015>
- 900 Bejannin, S., van Beek, P., Stieglitz, T., Souhaut, M., Tamborski, J., 2017. Combining
901 airborne thermal infrared images and radium isotopes to study submarine
902 groundwater discharge along the French Mediterranean coastline. *J. Hydrol. Reg.*
903 *Stud.* 13, 72–90. <https://doi.org/10.1016/J.EJRH.2017.08.001>
- 904 Berg, R.R., 1970. Method for Determining Permeability from Reservoir Rock Properties
905 20.
- 906 Bhaskar, A.S., Harvey, J.W., Henry, E.J., 2012. Resolving hyporheic and groundwater
907 components of streambed water flux using heat as a tracer. *Water Resour. Res.* 48.

908 <https://doi.org/10.1029/2011WR011784>

909 Boano, F., Harvey, J.W., Marion, A., Packman, A.I., Revelli, R., Ridolfi, L., Wörman, A., 2014.

910 Hyporheic flow and transport processes: Mechanisms, models, and biogeochemical

911 implications. *Rev. Geophys.* 52, 603–679. <https://doi.org/10.1002/2012RG000417>

912 Bokuniewicz, H., Pollock, M., Blum, J., Wilson, R., 2004. Submarine Ground Water

913 Discharge and Salt Penetration Across the Sea Floor. *Ground Water* 42, 983–989.

914 <https://doi.org/10.1111/j.1745-6584.2004.tb02637.x>

915 Caldwell, D.R., 1974. Thermal conductivity of sea water. *Deep Sea Res. Oceanogr. Abstr.*

916 21, 131–137. [https://doi.org/10.1016/0011-7471\(74\)90070-9](https://doi.org/10.1016/0011-7471(74)90070-9)

917 Cardenas, M.B., Jiang, H., 2011. Wave-driven porewater and solute circulation through

918 rippled elastic sediment under highly transient forcing. *Limnol. Oceanogr. Fluids*

919 *Environ.* 1, 23–37. <https://doi.org/10.1215/21573698-1151658>

920 Charette, M.A., Allen, M.C., 2006. Precision Ground Water Sampling in Coastal Aquifers

921 Using a Direct-Push, Shielded-Screen Well-Point System. *Gr. Water Monit. Remediat.*

922 26, 87–93. <https://doi.org/10.1111/j.1745-6592.2006.00076.x>

923 Cho, H.-M., Kim, G., Kwon, E.Y., Moosdorf, N., Garcia-Orellana, J., Santos, I.R., 2018. Radium

924 tracing nutrient inputs through submarine groundwater discharge in the global

925 ocean. *Sci. Rep.* 8, 2439. <https://doi.org/10.1038/s41598-018-20806-2>

926 Cook, P.G., Rodellas, V., Andrisoa, A., Stieglitz, T.C., 2018a. Exchange across the sediment-

927 water interface quantified from porewater radon profiles. *J. Hydrol.* 559, 873–883.

928 <https://doi.org/10.1016/j.jhydrol.2018.02.070>

929 Cook, P.G., Rodellas, V., Stieglitz, T.C., 2018b. Quantifying Surface Water, Porewater and

930 Groundwater Interactions Using Tracers: Tracer Fluxes, Water Fluxes and

931 Endmember Concentrations. *Water Resour. Res.*

932 <https://doi.org/10.1002/2017WR021780>

- 933 Cranswick, R.H., Cook, P.G., Lamontagne, S., 2014. Hyporheic zone exchange fluxes and
934 residence times inferred from riverbed temperature and radon data. *J. Hydrol.* 519,
935 1870–1881. <https://doi.org/10.1016/J.JHYDROL.2014.09.059>
- 936 Duque, C., Müller, S., Sebok, E., Haider, K., Engesgaard, P., 2016. Estimating groundwater
937 discharge to surface waters using heat as a tracer in low flux environments: the role
938 of thermal conductivity. *Hydrol. Process.* 30, 383–395.
939 <https://doi.org/10.1002/hyp.10568>
- 940 Fiandrino, A., Giraud, A., Robin, S., Pinatel, C., 2012. Validation d'une méthode
941 d'estimation des volumes d'eau échangés entre la mer et les lagunes et définition
942 d'indicateurs hydrodynamiques associés.
- 943 Garcés, E., Basterretxea, G., Tovar-Sánchez, A., 2011. Changes in microbial communities in
944 response to submarine groundwater input. *Mar. Ecol. Prog. Ser.* 438, 47–58.
945 <https://doi.org/10.3354/meps09311>
- 946 Gelhar, L.W., Welty, C., Rehfeldt, K.R., 1992. A critical review of data on field-scale
947 dispersion in aquifers. *Water Resour. Res.* 28, 1955–1974.
948 <https://doi.org/10.1029/92WR00607>
- 949 Gobler, C., Sañudo-Wilhelmy, S., 2001. Temporal variability of groundwater seepage and
950 brown tide blooms in a Long Island embayment. *Mar. Ecol. Prog. Ser.* 217, 299–309.
- 951 Gonnee, M.E., Mulligan, A.E., Charette, M.A., 2013. Climate-driven sea level anomalies
952 modulate coastal groundwater dynamics and discharge. *Geophys. Res. Lett.* 40,
953 2701–2706. <https://doi.org/10.1002/grl.50192>
- 954 Heiss, J.W., Post, V.E.A., Laattoe, T., Russoniello, C.J., Michael, H.A., 2017. Physical Controls
955 on Biogeochemical Processes in Intertidal Zones of Beach Aquifers. *Water Resour.*
956 *Res.* 53, 9225–9244. <https://doi.org/10.1002/2017WR021110>
- 957 Huettel, M., Berg, P., Kostka, J.E., 2014. Benthic exchange and biogeochemical cycling in

958 permeable sediments. *Ann. Rev. Mar. Sci.* 6, 23–51.
959 <https://doi.org/10.1146/annurev-marine-051413-012706>

960 Hwang, D.W., Lee, Y.W., Kim, G., 2005. Large submarine groundwater discharge and
961 benthic eutrophication in Bangdu Bay on volcanic Jeju Island, Korea. *Limnol.*
962 *Oceanogr.* 50, 1393–1403.

963 Irvine, D., Simmons, C., Werner, A., Graf, T., 2015. Heat and solute tracers: how do they
964 compare in heterogeneous aquifers? *Ground Water* 53, 10–20.
965 <https://doi.org/10.1111/gwat.12146>

966 Johnson, A.N., Boer, B.R., Woessner, W.W., Stanford, J.A., Poole, G.C., Thomas, S.A., O’Daniel,
967 S.J., 2005. Evaluation of an Inexpensive Small-Diameter Temperature Logger for
968 Documenting Ground Water-River Interactions. *Gr. Water Monit. Remediat.* 25, 68–
969 74. <https://doi.org/10.1111/j.1745-6592.2005.00049.x>

970 King, J.N., 2012. Synthesis of benthic flux components in the Patos Lagoon coastal zone,
971 Rio Grande do Sul, Brazil. *Water Resour. Res.* 48.
972 <https://doi.org/10.1029/2011WR011477>

973 King, J.N., Mehta, A.J., Dean, R.G., 2009. Generalized analytical model for benthic water flux
974 forced by surface gravity waves. *J. Geophys. Res.* 114, C04004.
975 <https://doi.org/10.1029/2008JC005116>

976 Kwon, E.Y., Kim, G., Primeau, F., Moore, W.S., Cho, H.-M., DeVries, T., Sarmiento, J.L.,
977 Charette, M.A., Cho, Y.-K., 2014. Global estimate of submarine groundwater discharge
978 based on an observationally constrained radium isotope model. *Geophys. Res. Lett.*
979 n/a-n/a. <https://doi.org/10.1002/2014GL061574>

980 Lamontagne, S., Cosme, F., Minard, A., Holloway, A., 2018. Nitrogen attenuation, dilution
981 and recycling in the intertidal hyporheic zone of a subtropical estuary. *Hydrol. Earth*
982 *Syst. Sci.* 22, 4083–4096. <https://doi.org/10.5194/hess-22-4083-2018>

983 Lee, E., Hyun, Y., Lee, K.-K., 2013. Sea level periodic change and its impact on submarine
984 groundwater discharge rate in coastal aquifer. *Estuar. Coast. Shelf Sci.* 121–122, 51–
985 60. <https://doi.org/10.1016/j.ecss.2013.02.011>

986 Lee, Y.W., Kim, G., Lim, W.A., Hwang, D.W., 2010. A relationship between submarine
987 groundwater-borne nutrients traced by Ra isotopes and the intensity of
988 dinoflagellate red-tides occurring in the southern sea of Korea. *Limnol. Oceanogr.* 55,
989 1–10.

990 Li, L., Barry, D., 2000. Wave-induced beach groundwater flow. *Adv. Water Resour.* 23,
991 325–337. [https://doi.org/10.1016/S0309-1708\(99\)00032-9](https://doi.org/10.1016/S0309-1708(99)00032-9)

992 Li, Y., Šimůnek, J., Wang, S., Zhang, W., Yuan, J., 2017. Simulating the Effects of Lake Wind
993 Waves on Water and Solute Exchange across the Lakeshore Using Hydrus-2D. *Water*
994 9, 566. <https://doi.org/10.3390/w9080566>

995 Liefer, J.D., MacIntyre, H.L., Su, N., Burnett, W.C., 2013. Seasonal Alternation Between
996 Groundwater Discharge and Benthic Coupling as Nutrient Sources in a Shallow
997 Coastal Lagoon. *Estuaries and Coasts* 37, 1–16. [https://doi.org/10.1007/s12237-](https://doi.org/10.1007/s12237-013-9739-4)
998 013-9739-4

999 Martin, J.B., Cable, J.E., Jaeger, J., Hartl, K., Smith, C.G., 2006. Thermal and chemical
1000 evidence for rapid water exchange across the sediment-water interface by
1001 bioirrigation in the Indian River Lagoon, Florida. *Limnol. Oceanogr.* 51, 1332–1341.
1002 <https://doi.org/10.4319/lo.2006.51.3.1332>

1003 Martin, J.B., Cable, J.E., Smith, C., Roy, M., Cherrier, J., 2007. Magnitudes of submarine
1004 groundwater discharge from marine and terrestrial sources: Indian River Lagoon,
1005 Florida. *Water Resour. Res.* 43, n/a-n/a. <https://doi.org/10.1029/2006WR005266>

1006 Martin, J.B., Cable, J.E., Swarzenski, P.W., Lindenberg, M.K., 2004. Enhanced Submarine
1007 Ground Water Discharge from Mixing of Pore Water and Estuarine Water. *Ground*

1008 Water 42, 1000–1010. <https://doi.org/10.1111/j.1745-6584.2004.tb02639.x>

1009 Michael, H.A., Mulligan, A.E., Harvey, C.F., 2005. Seasonal oscillations in water exchange
1010 between aquifers and the coastal ocean. *Nature* 436, 1145–8.
1011 <https://doi.org/10.1038/nature03935>

1012 Michael, H.A., Russoniello, C.J., Byron, L.A., 2013. Global assessment of vulnerability to
1013 sea-level rise in topography-limited and recharge-limited coastal groundwater
1014 systems. *Water Resour. Res.* 49, 2228–2240. <https://doi.org/10.1002/wrcr.20213>

1015 Molina-Giraldo, N., Bayer, P., Thermal, P.B.-I.J. of, 2011, undefined, 2011. Evaluating the
1016 influence of thermal dispersion on temperature plumes from geothermal systems
1017 using analytical solutions. *Int. J. Therm. Sci.* 50, 1223–1231.
1018 <https://doi.org/doi.org/10.1016/j.ijthermalsci.2011.02.004>

1019 Moore, W.S., 2010. The Effect of Submarine Groundwater Discharge on the Ocean. *Ann.*
1020 *Rev. Mar. Sci.* 2, 59–88. <https://doi.org/10.1146/annurev-marine-120308-081019>

1021 Moore, W.S., Sarmiento, J.L., Key, R.M., 2008. Submarine groundwater discharge revealed
1022 by ^{228}Ra distribution in the upper Atlantic Ocean. *Nat. Geosci.* 1, 309–311.
1023 <https://doi.org/10.1038/ngeo183>

1024 Morris, J.T., 1995. The Mass Balance of Salt and Water in Intertidal Sediments: Results
1025 from North Inlet, South Carolina. *Estuaries* 18, 556.
1026 <https://doi.org/10.2307/1352376>

1027 Nash, S.G., 1984. Newton-Type Minimization via the Lanczos Method. *SIAM J. Numer.*
1028 *Anal.* 21, 770–788. <https://doi.org/10.1137/0721052>

1029 Oliphant, T.E., 2007. Python for Scientific Computing. *Comput. Sci. Eng.* 9, 10–20.
1030 <https://doi.org/10.1109/MCSE.2007.58>

1031 Paerl, H., 1997. Coastal eutrophication and harmful algal blooms: Importance of
1032 atmospheric deposition and groundwater as "new" nitrogen and other nutrient

- 1033 sources. *Limnol. Oceanogr.* 42, 1154–65.
- 1034 Precht, E., Huettel, M., 2003. Advective pore-water exchange driven by surface gravity
1035 waves and its ecological implications. *Limnol. Oceanogr.* 48, 1674–1684.
1036 <https://doi.org/10.4319/lo.2003.48.4.1674>
- 1037 Qian, Q., Clark, J.J., Voller, V.R., Stefan, H.G., 2009. Depth-Dependent Dispersion Coefficient
1038 for Modeling of Vertical Solute Exchange in a Lake Bed under Surface Waves. *J.*
1039 *Hydraul. Eng.* 135, 187–197. [https://doi.org/10.1061/\(ASCE\)0733-](https://doi.org/10.1061/(ASCE)0733-9429(2009)135:3(187))
1040 [9429\(2009\)135:3\(187\)](https://doi.org/10.1061/(ASCE)0733-9429(2009)135:3(187))
- 1041 Rapaglia, J.P., Bokuniewicz, H.J., 2009. The effect of groundwater advection on salinity in
1042 pore waters of permeable sediments. *Limnol. Oceanogr.* 54, 630–643.
- 1043 Rau, G.C., Andersen, M.S., Acworth, R.I., 2012. Experimental investigation of the thermal
1044 dispersivity term and its significance in the heat transport equation for flow in
1045 sediments. *Water Resour. Res.* 48. <https://doi.org/10.1029/2011WR011038>
- 1046 Rau, G.C., Andersen, M.S., McCallum, A.M., Roshan, H., Acworth, R.I., 2014. Heat as a tracer
1047 to quantify water flow in near-surface sediments. *Earth-Science Rev.* 129, 40–58.
1048 <https://doi.org/10.1016/j.earscirev.2013.10.015>
- 1049 Robinson, C., Xin, P., Li, L., Barry, D.A., 2014. Groundwater flow and salt transport in a
1050 subterranean estuary driven by intensified wave conditions. *Water Resour. Res.* 50,
1051 165–181. <https://doi.org/10.1002/2013WR013813>
- 1052 Robinson, C.E., Xin, P., Santos, I.R., Charette, M.A., Li, L., Barry, D.A., 2017. Groundwater
1053 dynamics in subterranean estuaries of coastal unconfined aquifers: Controls on
1054 submarine groundwater discharge and chemical inputs to the ocean. *Adv. Water*
1055 *Resour.* <https://doi.org/10.1016/j.advwatres.2017.10.041>
- 1056 Rodellas, V., Garcia-Orellana, J., Masqué, P., Feldman, M., Weinstein, Y., 2015. Submarine
1057 groundwater discharge as a major source of nutrients to the Mediterranean Sea.

1058 Proc. Natl. Acad. Sci. U. S. A. 112, 3926–30.
1059 <https://doi.org/10.1073/pnas.1419049112>

1060 Rodellas, V., Garcia-Orellana, J., Trezzi, G., Masqué, P., Stieglitz, T.C., Bokuniewicz, H.,
1061 Cochran, J.K., Berdalet, E., 2017. Using the radium quartet to quantify submarine
1062 groundwater discharge and porewater exchange. *Geochim. Cosmochim. Acta* 196.
1063 <https://doi.org/10.1016/j.gca.2016.09.016>

1064 Rodellas, V., Stieglitz, T.C., Andrisoa, A., Cook, P.G., Raimbault, P., Tamborski, J.J., van Beek,
1065 P., Radakovitch, O., 2018. Groundwater-driven nutrient inputs to coastal lagoons:
1066 The relevance of lagoon water recirculation as a conveyor of dissolved nutrients. *Sci.*
1067 *Total Environ.* 642, 764–780. <https://doi.org/10.1016/j.scitotenv.2018.06.095>

1068 Santos, I.R., Burnett, W.C., Chanton, J., Dimova, N., Peterson, R.N., 2009. Land or ocean?:
1069 Assessing the driving forces of submarine groundwater discharge at a coastal site in
1070 the Gulf of Mexico. *J. Geophys. Res.* 114, C04012.
1071 <https://doi.org/10.1029/2008JC005038>

1072 Santos, I.R., Eyre, B.D., Huettel, M., 2012. The driving forces of porewater and
1073 groundwater flow in permeable coastal sediments: A review. *Estuar. Coast. Shelf Sci.*
1074 98, 1–15. <https://doi.org/10.1016/j.ecss.2011.10.024>

1075 Savidge, W.B., Wilson, A., Woodward, G., 2016. Using a Thermal Proxy to Examine
1076 Sediment–Water Exchange in Mid-Continental Shelf Sandy Sediments. *Aquat.*
1077 *Geochemistry* 22, 419–441. <https://doi.org/10.1007/s10498-016-9295-1>

1078 Sawyer, A.H., Shi, F., Kirby, J.T., Michael, H.A., 2013. Dynamic response of surface water-
1079 groundwater exchange to currents, tides, and waves in a shallow estuary. *J. Geophys.*
1080 *Res. Ocean.* 118, 1749–1758. <https://doi.org/10.1002/jgrc.20154>

1081 Simmons, C.T., Fenstemaker, T.R., Sharp, J.M., 2001. Variable-density groundwater flow
1082 and solute transport in heterogeneous porous media: approaches, resolutions and

1083 future challenges. *J. Contam. Hydrol.* 52, 245–275. <https://doi.org/10.1016/S0169->
1084 [7722\(01\)00160-7](https://doi.org/10.1016/S0169-7722(01)00160-7)

1085 Smith, C.G., Cable, J.E., .Martin, J.B., 2008. Episodic high intensity mixing events in a
1086 subterranean estuary: Effects of tropical cyclones. *Limnol. Oceanogr.* 53, 666–674.
1087 <https://doi.org/10.4319/lo.2008.53.2.0666>

1088 Sous, D., Petitjean, L., Bouchette, F., Rey, V., Meulé, S., Sabatier, F., Martins, K., 2016. Field
1089 evidence of swash groundwater circulation in the microtidal rousty beach, France.
1090 *Adv. Water Resour.* 97, 144–155.
1091 <https://doi.org/10.1016/J.ADVWATRES.2016.09.009>

1092 Stieglitz, T.C., Beek, P., Souhaut, M., Cook, P.G., 2013. Karstic groundwater discharge and
1093 seawater recirculation through sediments in shallow coastal Mediterranean lagoons,
1094 determined from water, salt and radon budgets. *Mar. Chem.* 156, 73–84.
1095 <https://doi.org/10.1016/j.marchem.2013.05.005>

1096 Sugimoto, R., Honda, H., Kobayashi, S., Takao, Y., Tahara, D., Tominaga, O., Taniguchi, M.,
1097 2015. Seasonal Changes in Submarine Groundwater Discharge and Associated
1098 Nutrient Transport into a Tideless Semi-enclosed Embayment (Obama Bay, Japan).
1099 *Estuaries and Coasts.* <https://doi.org/10.1007/s12237-015-9986-7>

1100 Tamborski, J., Bejannin, S., Garcia-Orellana, J., Souhaut, M., Charbonnier, C., Anschutz, P.,
1101 Pujo-Pay, M., Conan, P., Crispi, O., Monnin, C., Stieglitz, T., Rodellas, V., Andrisoa, A.,
1102 Claude, C., van Beek, P., 2018. A comparison between water circulation and
1103 terrestrially-driven dissolved silica fluxes to the Mediterranean Sea traced using
1104 radium isotopes. *Geochim. Cosmochim. Acta* 238, 496–515.
1105 <https://doi.org/10.1016/J.GCA.2018.07.022>

1106 Valiela, I., Costa, J., Foreman, K., Teal, J.M., Howes, B., Aubrey, D., 1990. Transport of
1107 groundwater-borne nutrients from watersheds and their effects on coastal waters.

1108 Biogeochemistry 10, 177–197. <https://doi.org/10.1007/BF00003143>

1109 van der Walt, S.S., Colbert, S.C., Varoquaux, G.G., 2011. The NumPy Array: A Structure for
1110 Efficient Numerical Computation. *Comput. Sci. Eng.* 13, 22–30.
1111 <https://doi.org/10.1109/MCSE.2011.37>

1112 Voss, C.I., Souza, W.R., 1987. Variable density flow and solute transport simulation of
1113 regional aquifers containing a narrow freshwater-saltwater transition zone. *Water*
1114 *Resour. Res.* 23, 1851–1866. <https://doi.org/10.1029/WR023i010p01851>

1115 Weinstein, Y., Yechieli, Y., Shalem, Y., Burnett, W.C., Swarzenski, P.W., Herut, B., 2011.
1116 What is the role of fresh groundwater and recirculated seawater in conveying
1117 nutrients to the coastal ocean? *Environ. Sci. Technol.* 45, 5195–200.
1118 <https://doi.org/10.1021/es104394r>

1119 Whipple, A.C., Luettich, R.A., Reynolds-Fleming, J. V., Neve, R.H., 2018. Spatial differences
1120 in wind-driven sediment resuspension in a shallow, coastal estuary. *Estuar. Coast.*
1121 *Shelf Sci.* 213, 49–60. <https://doi.org/10.1016/J.ECSS.2018.08.005>

1122 Wilke, M., Boutière, H., 2000. Synthèse générale du fonctionnement hydrobiologique de
1123 l'étang de La Palme, CEH. Perpignan, France.

1124 Wilson, A.M., Evans, T.B., Moore, W.S., Schutte, C.A., Joye, S.B., 2015. What time scales are
1125 important for monitoring tidally influenced submarine groundwater discharge?
1126 Insights from a salt marsh. *Water Resour. Res.* 51, 4198–4207.
1127 <https://doi.org/10.1002/2014WR015984>

1128 Wilson, A.M., Woodward, G.L., Savidge, W.B., 2016. Using heat as a tracer to estimate the
1129 depth of rapid porewater advection below the sediment–water interface. *J. Hydrol.*
1130 538, 743–753. <https://doi.org/10.1016/j.jhydrol.2016.04.047>

1131 Yu, X., Xin, P., Lu, C., Robinson, C., Li, L., Barry, D.A., 2017. Effects of episodic rainfall on a
1132 subterranean estuary. *Water Resour. Res.* 53, 5774–5787.

1133 <https://doi.org/10.1002/2017WR020809>

1134